Transport of a passive scalar at a shear-free boundary in fully developed turbulent open channel flow

R. A. Handler,[a] J. R. Saylor, R. I. Leighton, and A. L. Rovelstad[b]
Naval Research Laboratory, Washington, DC 20375

(Received 5 February 1999; accepted 14 May 1999)

Direct numerical simulations of fully developed turbulence in an open channel geometry were performed in which a passive scalar was introduced. The simulations were intended to explore transport at free surfaces in two cases for which (1) the free surface was maintained at constant temperature and (2) the interfacial flux was fixed. These cases can be considered models for mass and evaporative heat transport where buoyancy and surface deformation effects are negligible. Significant differences were found in the thermal fields in these two cases. The turbulent statistics reveal that the surface flux in the constant temperature case was significantly more intermittent compared to the surface temperature field in the constant flux case. The surface temperature field in the latter case formed large patches of warm fluid, reminiscent of the so-called *fish scale* patterns revealed in recent infrared imagery of the air–water interface. The wake-like structure of the patches was evident *despite* the absence of surface shear. A model of surface renewal based on the existence of two disparate time scales (a fast hydrodynamic scale, and a slow, diffusional scale) was introduced to explain these differences in a heuristic manner. The model appears successful in explaining, in a qualitative sense, the surface thermal structure in each case. Correlations between the surface thermal fields (flux or temperature) and the subsurface hydrodynamics were also computed. A model based on the hypothesis that hairpin eddies are the dominant kinematic structure responsible for surface renewal is consistent with the correlations. However, these results cannot rule out the importance of other turbulent structures in free surface heat and mass transport processes. © *1999 American Institute of Physics.* [S1070-6631(99)00309-8]

I. INTRODUCTION

The interaction of turbulence with a free surface has been under active investigation for at least the last two decades. This research has been motivated by the need for more fundamental knowledge of interfacial transport processes which may ultimately be used in developing physics-based interfacial transport models. Such models should be of importance in predicting, for example, the fluxes of heat and mass from the air–sea interface, the spreading of ship wakes, and the fluxes associated with numerous industrial processes.

Although there has been some fundamental work on sheared free surfaces,[1–3] this investigation is primarily concerned with the unsheared case. In some ways, this is the more fundamental example, since there can be no turbulence production at such an interface. A natural and convenient way to investigate these flows is through the use of an open channel where the turbulence which arrives at the free surface is produced principally at the bottom solid wall. Thus open channel flow has been used in many experimental and numerical investigations of turbulence-free surface interactions. In this work, which is principally concerned with the relationship between turbulent structure near the interface and the passive scalar or temperature field near it, open channel turbulence has also been used as the basis for the investigation.

To place the present work in context, the previous experimental and numerical research on open channel turbulence is briefly reviewed. Previous experimental work[4–7] has revealed that a very large fraction, possibly as high as 90% of the surface renewal events are due to *bursting* processes near the solid boundary. This was revealed by using dye tracers placed in the buffer region of the wall boundary layer and monitoring the presence of dye at the surface. This work has also verified that large-scale, energy-containing eddies, as opposed to dissipation scale motions, are primarily responsible for surface renewal. In addition, the experiments conclusively determined that the free surface transport coefficient scales well with the square root of the molecular diffusivity, in agreement with standard surface renewal models.[8–11]

Additional experiments[12–14] have revealed the existence of so-called surface renewal *patches* at the free surface. In particular, they have confirmed the experimental observations of Komori[6] that a large fraction of surface renewal events originate from the buffer region of the boundary layer and are closely correlated with boundary layer bursts. Based on this idea, a surface renewal model which incorporates the time scales associated with the patches can be developed. A relatively simple scenario emerges from these experiments; low-speed fluid is ejected toward the surface from a wall burst, the fluid rises to the surface to form a surface renewal

[a]Electronic mail: handler@raphael.nrl.navy.mil
[b]Present address: Corning Glass Corp., Corning, NY 14831.

patch, and a downdraft develops after the interaction. Additional work by Rashidi[14] has revealed the existence of spiral eddies or attached eddies which appear after an energetic surface renewal event.

The experimental work, although it has revealed much about the processes involved in turbulent surface renewal, has been plagued by considerable difficulty in making accurate velocity and scalar measurements very near the interface. To some extent, the advent of high-resolution numerical simulations has alleviated this problem, allowing precise determination of the velocity field very close to the free surface, at least for low Reynolds and Prandtl numbers. This work[15–18] has generally confirmed the direct relation between wall bursts and surface renewal and has revealed that the updrafts from bursting appear to be the important process, although other experimentaly observed structures such as down-drafts and attached or spiral eddies are seen as well. In addition, the numerical simulations have revealed that the redistribution of kinetic energy from the vertical to the horizontal components of velocity is due to pressure-strain correlations. Nagaosa and Saito[18] have recently shown that the surface renewal events are often associated with vortex dipoles, and in recent work, Nagaosa[19] has shown that shear layers which often eminate from the wall region are not important in the surface renewal process.

In contrast to previous investigations, the remote sensing aspects of a free surface cooled from above are of primary concern. The kinds of questions which arise in this context are: Given only thermal information at the free surface, what can be inferred about the subsurface hydrodynamics and the subsurface thermal structure? Can heat flux be determined from surface thermal imagery? Can free surface thermal imagery be inverted to determine the underlying bottom topography or the presence of underwater objects or obstructions? To answer these and related questions, the relationship between the surface scalar, or temperature field, and the underlying hydrodynamics needs to be determined in a well-defined case.

In particular, recent experiments[20,21] which have explored the use of recently developed infrared technology to determine the relationship between the free surface temperature field and the subsurface velocity field have supplied motivation for the current investigation. These experiments have relied upon recent developments in infrared focal plane array technology which allows for the determination of the temperature field with great thermal, spatial, and temporal resolution. Using these methods, the surface thermal signature of the thin thermal boundary layer, formed in the water by evaporative cooling, has been investigated in detail. This surface cooling naturally gives rise to a free surface temperature which is slightly lower than in the bulk. This layer, typically referred to as the *cool skin*[22–25] in the oceanographic context, will naturally be strongly affected by forced convection due to the wind. The boundary layer itself is not static, but is being maintained by surface renewal events from below. Once formed, however, it can be disrupted by coherent events such as, for example, a subsurface wake, which will generally be seen as a warm region in infrared imagery.[26]

Two cases were explored in this work: (1) open channel turbulence in which the free surface and the bottom boundary are maintained at constant temperature, with the bottom temperature greater than the top, and (2) open channel flow with a velocity field which is statistically identical to the first case, in which the free surface is subject to a constant outward (cooling) heat flux and the bottom wall is maintained at a fixed temperature. Buoyancy effects were not included in either case. It has been shown[18] that stable stratification in open channel flow significantly reduces the turbulence intensities, Reynolds stress, and drag. The cases considered here, however, would clearly be unstably stratified had buoyancy effects been included. In fact, the so-called *cool skin* is actually maintained by such a surface cooling which generates descending cold plumes and ascending warmer fluid. For the flows considered in the present investigation, however, a cool thermal boundary layer can be maintained at the free surface in the absence of buoyancy since *bursting* events from the no-slip lower boundary provide surface renewal in which cooler fluid from the free surface is swept clean and replaced by warmer fluid from below. The effects of unstable stratification will be considered in future work.

It should be mentioned here that case (1) should be a reasonable model for mass transport at a free surface as in the case of, for example, the outgassing of carbon dioxide from water to air.[27–29] In this case, an excellent approximation is that the gas concentration in the air and at the free surface remains constant. Since the Schmidt number of typical gases is much larger than one, it can easily be shown[30] that the subsurface hydrodynamics controls the gas flux or, in other words, the resistance to flux is greatest in the liquid. The second case—case (2)—more closely models heat transport in which evaporative cooling dominates. In this situation, the heat flux, which is controlled by the humidity and the wind, can be assumed to be held fixed to a close approximation in most situations.[20,21] Thus, the boundary conditions on the scalar fields in these two cases are reasonable models of turbulence mediated transport of mass and heat at the air–water interface, in the absence of significant surface deformations or buoyancy effects.

II. NUMERICAL SIMULATIONS

A. Problem formulation

To understand the basic mechanisms of scalar transport at free surfaces, direct numerical simulations were performed in which several simplifying assumptions are made. First, the *free surface* in these simulations is actually a shear-free interface in which no deformations are allowed. Estimates of the surface deformations for the strength of the flows considered here[5] indicate that they are negligible so that a flat boundary model is entirely appropriate. Second, as mentioned above, buoyancy effects were neglected. For simplicity, however, the passive scalar will be referred to as the *temperature* field.

Given these simplifying assumptions, the Navier–Stokes equations were solved in rotational form:

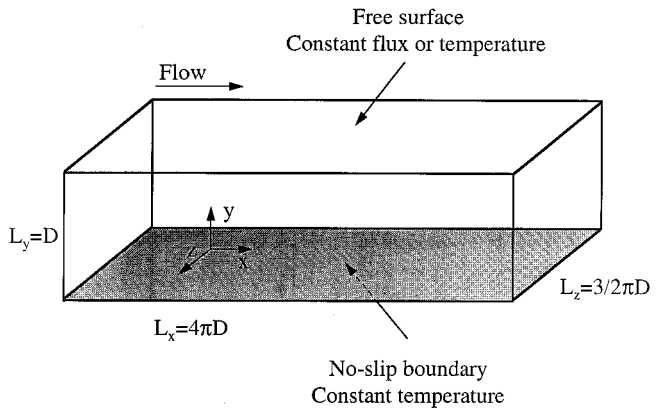

FIG. 1. Computational geometry and coordinate system.

$$\frac{\partial \mathbf{v}}{\partial t} = \mathbf{v}\times\boldsymbol{\Omega} - \nabla\Pi + \nu\nabla^2\mathbf{v} + \mathbf{f}/\rho, \tag{2.1}$$

where $\mathbf{v}$ is the velocity, $\boldsymbol{\Omega}=\boldsymbol{\nabla}\times\mathbf{v}$ is the vorticity, $\Pi = p/\rho + \frac{1}{2}(\mathbf{v}\cdot\mathbf{v})$, p is the pressure, ρ is the density, ν is the kinematic viscosity, $\mathbf{f}=f\hat{e}_x$ is a body force per unit volume, and $\hat{e}_x$ is a unit vector in the flow direction. In these simulations, the body force is a constant so as to represent a driving pressure gradient. In addition, the incompressibility constraint was enforced:

$$\boldsymbol{\nabla}\cdot\mathbf{v} = 0. \tag{2.2}$$

Cartesian coordinates (x,y,z) are used, where x and z are the planar or horizontal coordinates (in the plane of the free surface) and y is perpendicular to the boundary. The corresponding velocity field is (u,v,w). The computational domain is shown in Fig. 1.

The equations of motion can be nondimensionalized by choosing a length scale D, where D is the vertical extent of the channel, a velocity scale based on the pressure gradient, $u^* = \sqrt{|f|D/\rho}$, and a time scale, $t^* = D/u^*$. Introducing this scaling into (2.1) and (2.2) gives

$$\frac{\partial \mathbf{v}^+}{\partial \overline{t}} = \mathbf{v}^+\times\boldsymbol{\Omega}^+ - \boldsymbol{\nabla}\pi + \frac{1}{R^*}\nabla^2\mathbf{v}^+ + 1\hat{e}_x \tag{2.3}$$

and

$$\boldsymbol{\nabla}\cdot\mathbf{v}^+ = 0, \tag{2.4}$$

where $\mathbf{v}^+ = \mathbf{v}/u^* = (u^+,v^+,w^+)$, $\overline{t} = t/t^*$, $\boldsymbol{\Omega}^+ = \boldsymbol{\Omega}t^*$, $\pi = \Pi/\rho u^{*2}$, $R^* = u^*D/\nu$, and the nondimensional coordinates are $\overline{x} = x/D$, $\overline{y} = y/D$, and $\overline{z} = z/D$.

The boundary conditions which are applied at $\overline{y} = +1$ are those for a shear-free interface:

$$v^+ = 0 \tag{2.5}$$

and

$$\frac{\partial u^+}{\partial \overline{x}} = \frac{\partial w^+}{\partial \overline{z}} = 0, \tag{2.6}$$

where (2.5) expresses the zero deformation condition, and (2.6) enforces the absence of shear. The no-slip condition, $(u^+,v^+,w^+)=0$, is applied at $\overline{y}=0$.

Along with the equations of motion, the convection diffusion equation is solved for the temperature field and is given by

$$\frac{\partial \Theta^*}{\partial \overline{t}} + u^+\frac{\partial \Theta^*}{\partial \overline{x}} + v^+\frac{\partial \Theta^*}{\partial \overline{y}} + w^+\frac{\partial \Theta^*}{\partial \overline{z}} = \frac{1}{R^*\mathrm{Pr}}\nabla^2\Theta^*, \tag{2.7}$$

where Θ^* is a nondimensional temperature to be defined, $\mathrm{Pr} = \nu/\alpha$ is the Prandtl number, and α is the thermal diffusivity.

As described above, the present work is focused on two cases which model mass transport and evaporative heat transport at an interface. These cases can be modeled numerically by imposing, respectively, Dirichlet and Neumann boundary conditions on the temperature field. For the case in which Dirichlet conditions are imposed, which will be referred to as the constant temperature case, Θ^* will be defined as

$$\Theta^* = (\Theta - \Theta_T)/(|\Theta_B - \Theta_T|), \tag{2.8}$$

where Θ is the temperature, and Θ_T and Θ_B are the temperatures at the top and bottom boundaries respectively. In this case, the boundary conditions

$$\Theta^* = 0, \quad \overline{y} = 1 \tag{2.9}$$

and

$$\Theta^* = 1, \quad \overline{y} = 0 \tag{2.10}$$

will be imposed. In the other case, which will be referred to as the constant flux case, the nondimensional temperature is defined as $\Theta^* = [(\Theta - \Theta_B)k]/(q_0 D)$, where k is the thermal conductivity and q_0 is the magnitude of the heat flux directed normal to the interface applied at $\overline{y}=1$. The boundary conditions in this case are therefore given by

$$\frac{\partial \Theta^*}{\partial \overline{y}} = -1, \quad \overline{y} = 1, \tag{2.11}$$

$$\Theta^* = 0, \qquad \overline{y} = 0, \tag{2.12}$$

which are equivalent to a constant heat flux with magnitude q_0, directed out of the top boundary, and a constant temperature, Θ_B, maintained at the bottom boundary, respectively.

It is evident that in both the constant temperature and the constant flux cases, the heat transport is always directed out of the top boundary. In particular, as mentioned above, the constant temperature case has a close analogy with physical experiments in which a scalar such as a gas diffuses out of a liquid into the atmosphere. In this case, the atmosphere very closely approximates an infinite reservoir of fixed gas concentration so that the Dirichlet condition is an excellent approximation. On the other hand, the constant flux case approximates, with the exception of the absence of buoyancy, the physical situation in which the surface of the liquid is being cooled from above by evaporation. In this case, assuming the environment is maintained at constant humidity and

wind speed, the heat flux should remain nearly constant so that the Neumann condition should be appropriate.

B. Numerical methods

The simulations are carried out using the same procedure outlined by Handler *et al.*[16] in which a fourth-order system is solved for the vertical velocity and a second-order system is solved for the vertical vorticity. The other components of velocity are recovered from the imposition of continuity.

With this formulation, two boundary conditions are used for v on each boundary. The condition at $\overline{y}=1$ is

$$v^+=0, \quad \partial^2 v^+/\partial^2\overline{y}=0, \tag{2.13}$$

and on $\overline{y}=0$,

$$v^+=0, \quad \partial v^+/\partial\overline{y}=0. \tag{2.14}$$

The equations of motion were solved simultaneously with the heat transfer equation using a pseudo-spectral approach in which the velocity and temperature fields are expanded in Fourier modes in $\overline{x}$ and $\overline{z}$ and Chebyshev modes in $\overline{y}$. The fourth-order system for w^+ is solved using a Green's function approach.[31,32] Crank Nicolson time stepping is used for the diffusion operator and a second-order Adams–Bashforth scheme is used for the nonlinear terms. The Courant–Friedrichs–Lewy (CFL) number, defined by

$$\mathrm{CFL}=\Delta\overline{t}\max_{(\overline{x},\overline{z})}\left[\frac{|u^+|}{\Delta\overline{x}}+\frac{|v^+|}{\Delta\overline{y}}+\frac{|w^+|}{\Delta\overline{z}}\right], \tag{2.15}$$

remained below approximately 0.25 in each simulation. The calculations for the velocity and temperature were fully dealiased in the Fourier direction using the $\frac{3}{2}$'s rule.

The Reynolds number (R*) and the Prandtl number were 180 and 2, respectively, in all simulations. The resolution was $128\times129\times128$ in the x, y, and z directions, respectively, and the corresponding domain lengths were $L_x/D=4\pi$, $L_y/D=1$, and $L_z/D=3\pi/2$. If an inner or viscous length scale is defined by $l^+=\nu/u^*$, then in these units the domain is $2262\times180\times848$. The corresponding grid resolution in inner units in the x and z directions are 17.7 and 6.6, respectively. Length scales made nondimensional in this way will be denoted with a superscript $+$, such as $x^+=(xu^*)/\nu$.

III. TURBULENCE STATISTICS

The simulations were performed by first interpolating a lower resolution realization of fully developed turbulent open channel flow[16] onto the higher resolution ($128\times129\times128$) grid. This realization, along with temperature profiles corresponding to the case of pure conduction ($\Theta^*=-\overline{y}+1$, and $\Theta^*=-\overline{y}$ in the constant temperature case and constant flux case respectively) were used as initial conditions. Each simulation was then run for more than 100 large eddy turnover times until both the velocity field and the temperature field reached statistical equilibrium. The large integration time required to reach equilibrium is principally due to the Prandtl number being larger than one so that diffusion time scales for the temperature field are significantly longer than the scales associated with momentum transport. Once equilibrium is established, statistics were obtained for runs with a duration of about 30 large eddy turnover times. Also, since the temperature and velocity fields are uncoupled in these simulations, the velocity field statistics were virtually identical in both cases. Consequently, only the velocity statistics for the constant temperature case are presented.

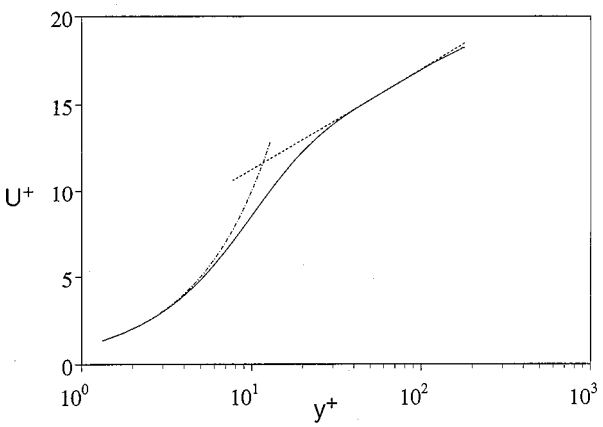

FIG. 2. Mean velocity profile and law of the wall. Computed mean velocity (U^+), –; $U^+=2.5\ln(y^+)+5.5$, – – –; $U^+=y^+$, –·–.

A. Velocity statistics

The results of previous investigations[16–18] at lower Reynolds numbers indicate, as expected, that the velocity statistics near the no-slip boundary are not affected by the existence of a free surface. The mean velocity profile, $U^+=\overline{u^+}$, is shown in Fig. 2. As expected from previous simulations, the law of the wall is obeyed reasonably well. There is a slight deviation from the classic logarithmic region in the wall law for $y^+>100$ which must be assumed to be due to the presence of the free surface. The bulk Reynolds number, $\mathrm{R}_b=U_bD/\nu=2805$, where U_b is the volume average velocity, and the centerline Reynolds number $\mathrm{R}_{\mathrm{cl}}=U_{\mathrm{cl}}D/\nu=3282$, where U_{cl} is the centerline velocity. These values are in reasonable agreement with the experimental values of Dean[33] for standard channel flow which are 2771 and 3236, respectively.

The turbulence intensity profiles are shown in Fig. 3. A

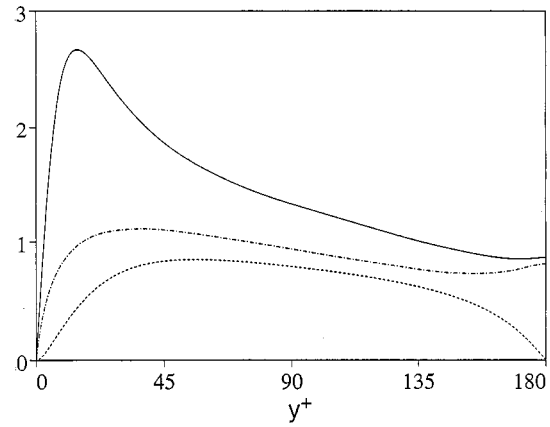

FIG. 3. Root-mean-square velocity profiles normalized by the friction velocity (u^*). Streamwise velocity (u_{rms}), –; wall normal velocity (v_{rms}), – – –; spanwise velocity (w_{rms}), –·–.

primed quantity will denote a time-dependent one for which the mean has been removed (e.g., u' is the fluctuating streamwise velocity) and $u_{\rm rms}$ will denote a root-mean-square value. The turbulence intensities near the solid boundary, where turbulence production is a maximum, show characteristics in agreement with standard closed channel simulations.[32,34] It should be mentioned that, although turbulence is produced everywhere in this flow with the exception of the boundaries, an analysis of the turbulence kinetic energy balances derived from the current simulations reveal that the turbulence production in the region $72<y^+<180$ is at least one order of magnitude less than its peak value near the solid boundary. This is certainly in accordance with the experiments mentioned above which have shown that surface renewal events have their origin principally in the near-wall region of the boundary layer. In agreement with lower Reynolds number results,[16] the turbulence intensities show a strong anisotropy near the shear free boundary. Analysis of the turbulence kinetic energy and dissipation budgets[15,16,18,35,36] has revealed that that anisotropic dissipation and pressure-strain effects are principally responsible for this anisotropy. Near the free surface, the dissipation becomes anisotropic due to the nature of the shear-free interfacial boundary conditions. As a result, the vertical fluctuations are preferentially dissipated, leading to an increase in stress anisotropy.[36]

Recent visualizations of the flow in the vicinity of the free surface by Nagaosa and Saito[18] have, to some extent, confirmed that strong updrafts, or *splats*, are the principal hydrodynamic events associated with the redistribution of turbulence kinetic energy by pressure-strain effects. For such a splat, one can envision, in a rough way, a stagnation point flow in which low momentum fluid from below is driven against the free surface. For such a flow, positive pressure fluctuations are expected to be associated with a negative vertical strain, $\partial v/\partial y$, resulting in a *negative* value for $\overline{p(\partial v/\partial y)}$ which is the pressure-strain term in the kinetic energy balance for the vertical velocity fluctuations. This is in accordance with recent simulation results.[16] On the other hand, continuity requires antisplatting or descending motions from the surface. It is interesting to note that Nagaosa and Saito have been able to visualize such splatting events and frequently observe dipole or hairpin-like eddies near the free surface.

The Reynolds stress $\overline{u'v'}$ is shown in Fig. 4. It is evident that the relation between the Reynolds stress, viscous stress, and the driving pressure gradient given by

$$-\frac{\overline{u'v'}}{u^{*2}}+\frac{1}{\mathrm{R}^*}\frac{dU^+}{d\overline{y}}=(1-\overline{y}) \tag{3.1}$$

is well satisfied, indicating that a statistically steady state has been achieved and that the sample size used to compute second-order statistics is adequate. We note in passing that the limiting behavior of the Reynolds stress in the vicinity of the shear-free boundary should be similar to that near the centerline of a two-walled turbulent channel flow. This can

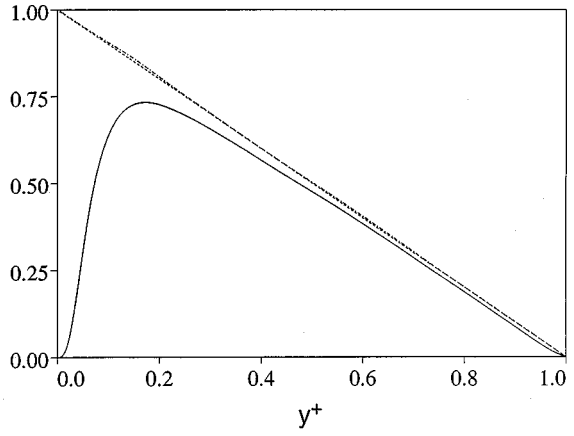

FIG. 4. Reynolds stress profile. Reynolds stress, $-\overline{u'v'}/u^{*2}$, $-$; mean momentum balance; $(1-\overline{y})$, $---$; $-\overline{u'v'}/u^{*2}+(1/R^*)(dU^+/d\overline{y})$, $-\cdot-$.

be seen by noting that the limiting behavior of the streamwise and vertical components of velocity near the free surface are given by

$$u'=a_0+a_2y^2+O(y^3), \tag{3.2}$$

$$v'=b_1y+b_3y^3+O(y^4), \tag{3.3}$$

where y denotes distance from the shear-free boundary. This leads to the limiting form of the Reynolds stress near the interface:

$$\overline{u'v'}=c_1y+c_3y^3+O(y^4). \tag{3.4}$$

Since the Reynolds stress for a two-walled channel must be odd with respect to the centerline, the limiting form of the stress in this case should be

$$\overline{u'v'}=d_1y+d_3y^3+O(y^5). \tag{3.5}$$

Thus, the shear-free boundary conditions do not appear to have an effect on the asymptotic behavior of the Reynolds stress, at least for the leading order terms.

The vorticity fluctuation profiles shown in Fig. 5 are in excellent agreement with results of Kim *et al.*[32] near the solid boundary ($0<y^+<50$) as expected and exhibit a local

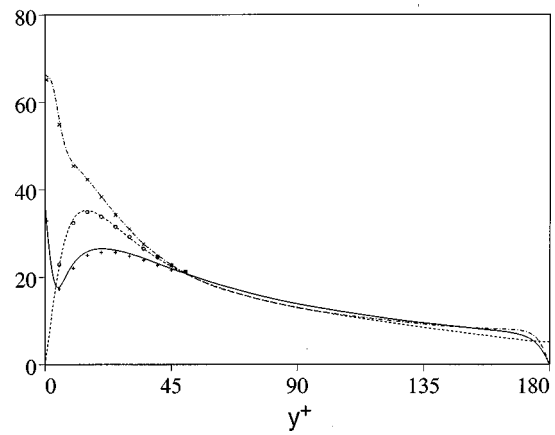

FIG. 5. Root-mean-square vorticity profiles. $\Omega_x^+=(\Omega_xD)/u^*$, $-$; Ω_y^+, $---$; Ω_z^+, $-\cdot-$. Results from Ref. 32, Ω_x^+, $+$; Ω_y^+, $\circ$; Ω_z^+, $\times$.

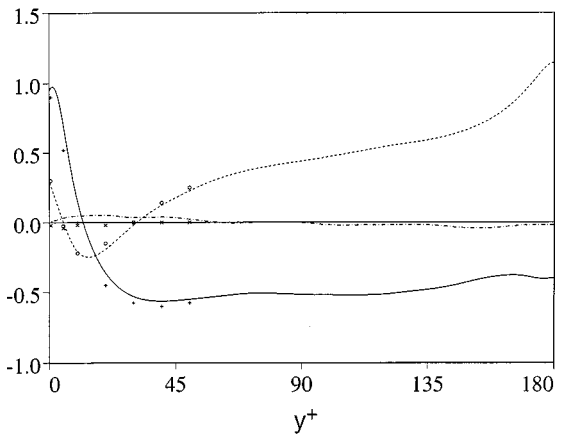

FIG. 6. Skewness for the velocity field. Streamwise velocity, $\overline{u'^3}/u_{\rm rms}^3$, –; wall normal velocity, $\overline{v'^3}/v_{\rm rms}^3$, – – –; spanwise velocity, $\overline{w'^3}/w_{\rm rms}^3$, -·-. Results from Ref. 32, $\overline{u'^3}/u_{\rm rms}^3$, +; $\overline{v'^3}/v_{\rm rms}^3$, ∘; $\overline{w'^3}/w_{\rm rms}^3$, ×.

minimum at $y^+\simeq 5$ in $\Omega_x)_{\rm rms}$, which has been interpreted as indicative of the existence of coherent streamwise vortices.[32] Near the free surface, the streamwise and spanwise vorticity intensities are seen to vanish, as they must, due to the stress-free conditions. There are no such limitations on the wall normal vorticity fluctuations, which attain a nonzero root-mean-square value at the interface. Thus, the existence of shear layers within the plane of the interface and attached vortices are kinematically possible, in addition to the splatting and antisplatting events mentioned above.

It is evident that the skewness and flatness profiles for all velocity components, shown in Figs. 6 and 7, are in excellent agreement with previous results[32] near the solid boundary. In addition, the skewness for w' is near zero everywhere, indicating that the sample size is at least marginally adequate for the computation of higher order statistics. From Fig. 6, it is clear that for $y^+>30$, the skewness for v' is always positive and that for u' is always negative. In fact, in the vicinity of the free surface (for $y^+>140$) the skewness for v' exhibits an increase and it attains a value of 1.16 at the interface.

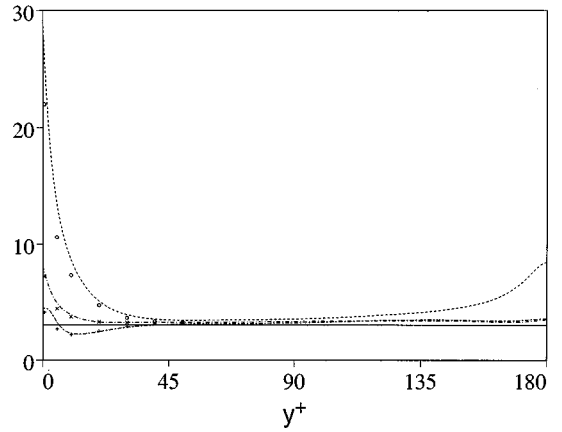

FIG. 7. Flatness for the velocity field. Gaussian result, –; streamwise velocity, $\overline{u'^4}/u_{\rm rms}^4$, —·—; wall normal velocity, $\overline{v'^4}/v_{\rm rms}^4$, – – –; spanwise velocity, $\overline{w'^4}/w_{\rm rms}^4$, -·-. Results from Ref. 32, $\overline{u'^4}/u_{\rm rms}^4$, +; $\overline{v'^4}/v_{\rm rms}^4$, ∘; $\overline{w'^4}/w_{\rm rms}^4$, ×.

Thus the largest number of intense motions near the interface are those for which the vertical velocity is positive (motion toward the surface) and the streamwise fluctuations are negative. This is certainly consistent with the experimental observations of ejections of low-speed fluid originating from the solid boundary impinging on the surface, giving rise to more intense splatting—as opposed to weaker antisplatting—motions. From Fig. 7 it is evident that near the shear-free boundary, the flatness for vertical velocity fluctuations, which attains a level of about 8, deviates significantly from Gaussian behavior. On the other hand, the flatness for the other velocity components deviates only slightly from Gaussian statistics.

B. Temperature statistics

The mean temperature profiles for the constant temperature and constant flux cases are shown in Fig. 8. Here the nondimensional temperature $\Theta^+=[(\Theta_B-\Theta)\rho c u^*]/q_0$ is used, where c is the heat capacity. It should be mentioned that the turbulence has markedly changed the initial mean scalar fields, which were set to be the theoretical conduction profiles. For example, in the constant temperature case, the magnitude of the nondimensional steady-state heat flux, $(q_0D)/[k(\Theta_B-\Theta_T)]$, is 7.64 compared to 1 in the case of pure conduction. For the constant flux case, the steady-state surface temperature $\overline{\Theta}^*=[(\overline{\Theta}-\Theta_B)k]/(q_0D)\simeq -0.133$, compared to the pure conduction case where $\Theta^*=-1$. Thus the effect of the turbulence has been to significantly increase the heat flux and to increase the surface temperature in the constant temperature and constant heat flux cases, respectively.

Kader[37] has developed a correlation for heat transfer in channels and boundary layers which appears to be reasonably accurate over a wide range of Prandtl and Reynolds numbers. As a means of comparison with Kader, a series of simulations were performed (not shown) for two-walled channel flow in which a spatially uniform heat source was introduced and each boundary was held at the same constant temperature. These simulations were similar to those performed by Kim.[38] The mean temperature profiles in these simulations, which were performed for a variety of Prandtl numbers, compared well with the Kader relation, thus validating our numerical integration of the heat equation. It is evident in Fig. 8, however, that the temperature profiles in both cases are very similar but agree with the Kader correlation only near the solid boundary for $y^+<15$. This is certainly to be expected since the Kader relation is valid only for geometries and boundary conditions which give rise to a symmetry in the temperature profile with respect to the centerline. Clearly, each case under consideration here violates this symmetry. Nevertheless, it is interesting to note that the temperature profiles obtained from the simulations exhibit a logarithmic region for $30<y^+<80$.

Unfortunately, there have been very few reliable measurements of heat or mass transport in open channel flows in the absence of surface shear. However, Rashidi *et al.*[13] have developed a simple model of surface renewal in open channel flows based on the the frequency of surface renewal

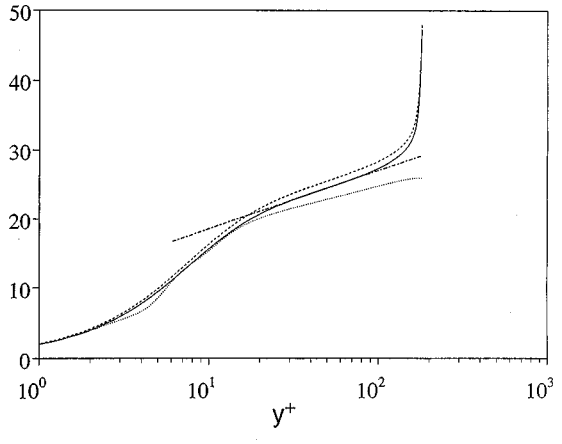

FIG. 8. Mean temperature profiles; $\overline{\Theta^+}=[(\Theta_B-\overline{\Theta})\rho c u^*]/q_0$. Constant temperature case, –; constant flux case, – – –; Ref. 37, ⋯; $\overline{\Theta^+}=3.68\ln(y^+)+10.1$, -·-.

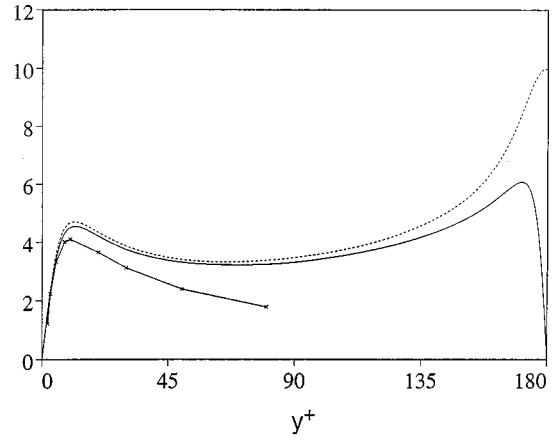

FIG. 9. Root-mean-square temperature profiles. Scaling for the temperature fluctuations is the same as for the mean temperature profiles in Fig. 8. Constant temperature case, –; constant flux case, – – –; Ref. 38, ×.

events emanating from bursting activity near the solid boundary. The model relies on the assumption that the transport coefficient should vary in inverse proportion to the square root of the Prandtl number, in accordance with standard surface renewal models. Their correlation, which agrees well with the experiments of Komori,[6] is given by

$$K_t \mathrm{Pr}^{1/2}/(U_b u^*)^{1/2}=7.7\times 10^{-3}, \tag{3.6}$$

where the heat transport coefficient is given by $K_t=q_0/[\rho c(\Theta_B-\Theta_T)]$. The relation between the bulk Reynolds number and the wall Reynolds number obtained from Dean[33] can be used to obtain an expression for the Nusselt number (Nu) from (3.6) given by

$$\mathrm{Nu}\ \mathrm{Pr}^{-1/2}=9.916\times 10^{-3}(\mathrm{R}^+)^{1.0714}, \tag{3.7}$$

where $\mathrm{Nu}=(K_t D)/\alpha$, and $\mathrm{R}^+=(2Du^*)/\nu$. For the conditions of the current simulations ($\mathrm{R}^+=360$, and $\mathrm{Pr}=2$), this relation predicts $\mathrm{Nu}=7.68$. This is in good agreement with $\mathrm{Nu}=7.64$ and 7.51 for the constant temperature and constant flux simulations, respectively. For comparison, $\mathrm{Nu}\simeq 14.4$ for the Kader model shown in Fig. 8. The lower Nusselt number for the current simulations compared to the Kader model is principally due to the existence of a sublayer ($175<y^+<180$) in the temperature profile near the free surface where molecular diffusion dominates. This sublayer is naturally absent in the case of standard channel or boundary layer flow. This additional layer apparently increases the resistance to heat flux by almost a factor of 2 as seen in the ratio of the Nusselt numbers. It should be mentioned, however, that the agreement between the current simulations and the experiments of Komori[6] should be taken with a degree of caution since Komori's experiments involved the transport of carbon dioxide with a very high Schmidt number ($\mathrm{Sc}\sim 400$) compared to the current simulations.

Nagaosa and Saito[18] have also performed a simulation of open channel flow with a passive scalar and report a Nusselt number of 11.3 for $\mathrm{Pr}=1$ and $\mathrm{R}^+=300$. The correlation (3.7) predicts a much lower transport rate, $\mathrm{Nu}=4.47$, under these flow conditions. This led to speculation by Nagaosa and Saito that the transport rate in the experiments was significantly affected by surfactant contamination which presumably dampened surface turbulence and decreases transport.[39] However, good agreement between the transport rates found in the current simulations and the experimental results lends some doubt to this contention. One possible reason for the discrepancy may be that Nagaosa and Saito used a transient simulation to compute the Nusselt number as opposed to the statistically steady state achieved in the current work. It is evident that additional physical and numerical experiments will be necessary to clarify this issue.

The root-mean-square temperature profiles for both cases are shown in Fig. 9. Near the solid boundary, the results appear to be in reasonable agreement with the simulation of Kim[38] in both amplitude and position of the local maximum. This is to be expected since Kim also used constant temperature boundary conditions on each wall of normal turbulent channel flow. Near the free surface, the fluctuations for the constant temperature case exhibit a local maximum away from the interface at $y^+\simeq 172$. For the constant flux case, there is no constraint on the temperature at the interface, and the temperature fluctuations are observed to reach a maximum there. In fact, the root-mean-square temperature fluctuation level at the free surface is about twice that of its local maximum near the solid boundary.

The convective heat flux ($\overline{\Theta' v'}$) profiles are shown in Fig. 10. A detailed quadrant analysis for this flux was not performed. However, as one would expect from the mean temperature profiles, the scalar fluxes are always positive; that is, fluid with $\Theta'>0$ tends to be strongly correlated with fluid rising from below ($v'>0$) and colder fluid ($\Theta'<0$) is associated with downward motions ($v'<0$). It was indicated above that there are small but noticeable differences in the mean temperature profiles for the two sets of boundary conditions being considered here. This can be explained in part by considering the asymptotic behavior of $\overline{\Theta' v'}$ near the free surface. At the free surface in the constant temperature case the temperature fluctuations can be expanded by,

$$\Theta'=e_1 y+e_2 y^2+O(y^3), \tag{3.8}$$

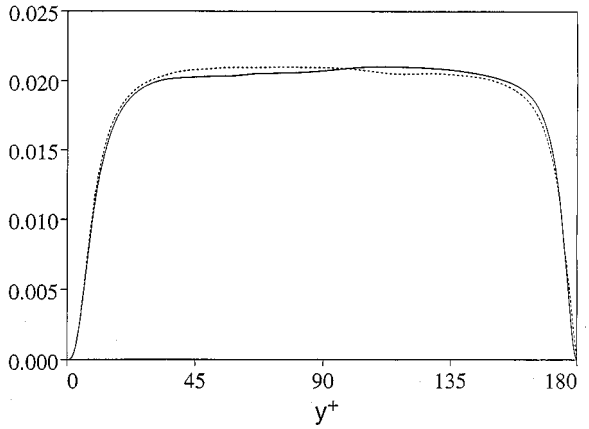

FIG. 10. Convective heat flux, $\overline{\Theta' v'}/[(\Theta_B-\Theta_T)u^*]$. Constant temperature case, –; constant flux case, – – –.

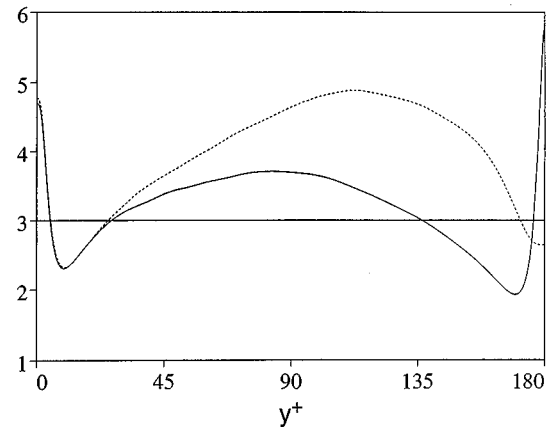

FIG. 12. Flatness for the temperature fluctuations; $\overline{\Theta'^4}/\Theta^4_{\rm rms}$. Gaussian result (flatness equals 3), –; Constant temperature case, –; constant flux case, – – –.

and in the constant flux case, the fluctuations can be expanded as

$$\Theta' = f_0 + f_2 y^2 + O(y^3). \tag{3.9}$$

Using the expression for the limiting forms of the vertical velocity fluctuations at the free surface given by (3.3), it follows that the asymptotic form for the scalar flux in the constant temperature case is

$$\overline{\Theta' v'} = Cy^2 + Dy^3 + O(y^4), \tag{3.10}$$

and for the constant flux case

$$\overline{\Theta' v'} = Ey + Fy^3 + O(y^4). \tag{3.11}$$

It is evident that the leading order terms for the heat flux near the free surface are different in these two cases. The differences indicated by (3.10) and (3.11) have been verified by a more careful inspection of the profiles shown in figure 10.

The skewness and flatness profiles for the temperature fluctuations for both cases are shown in Figs. 11 and 12. In general, these profiles indicate some significant differences, particularly near the free surface. The skewness for the temperature fluctuations in the constant temperature case is somewhat unanticipated. It should be noted that the flux $\overline{\Theta' v'}$ is strictly positive, so that, in the $\Theta' - v'$ plane, most events should occur in quadrants one ($\Theta'>0, v'>0$) or three ($\Theta'<0, v'<0$). Nevertheless, according to Fig. 10 and the skewness for v' from Fig. 6, there are only a few regions where the temperature and vertical velocity fluctuations have a skewness of the same sign. For example, for $165>y^+>50$ the skewness for Θ' is negative and that for v' is positive. This indicates that throughout a large region of the channel, the strongest vertical motions are not well correlated with the strongest fluctuations in the temperature field. This appears to be true also very near the wall for $y^+<6$. Near the free surface ($y^+>165$), however, the skewness for temperature and vertical velocity are both strongly positive, indicating that events in quadrant one dominate in the production of vertical flux in this region. For the constant flux case, the skewness for the temperature fluctuations remains, somewhat unexpectedly, slightly *negative* near the interface. The flatness profiles in Fig. 11 indicate that, for the constant temperature case, the strongest intermittency in the temperature field occurs very near the free surface. In contrast, the flatness level for the constant flux case is significantly non-Gaussian in the channel interior and is nearly Gaussian in the vicinity of the interface.

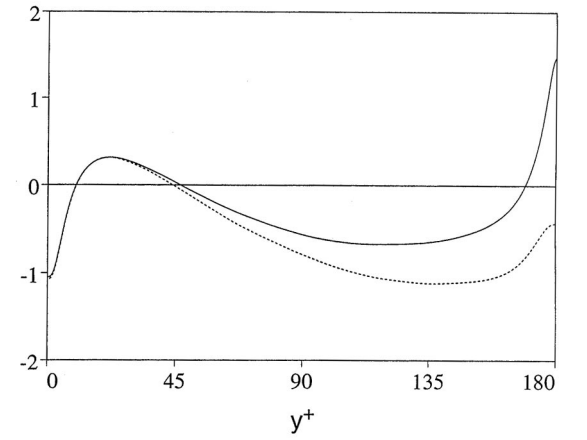

FIG. 11. Skewness for the temperature fluctuations; $\overline{\Theta'^3}/\Theta^3_{\rm rms}$. Constant temperature case, –; constant flux case, – – –.

For future reference, the integral scales for the thermal fields were computed at the free surface. Here we define the integral scale by $\Lambda_x = \int_0^{L_x/2} C_x(x')\,dx'$, where $C_x(x')$ is the spatial correlation function in the streamwise direction for the temperature defined by:

$$C_x(x') = \frac{\langle \Theta'(x-x')\Theta'(x)\rangle}{\Theta^2_{\rm rms}}, \tag{3.12}$$

where averaging is taken over the horizontal plane and all available realizations. The spanwise integral scales and those for the surface flux are defined in an analogous fashion. For the constant temperature case, the integral scale for the surface flux in the streamwise direction is $\Lambda_x/D = 0.274$ and in the spanwise direction $\Lambda_z/D = 0.229$. In the constant temperature case, the corresponding integral scales for the sur-

face temperature are 0.375 and 0.307. It is evident that the macroscales for the constant flux case are significantly larger than for the constant temperature case, and that the *aspect ratio* (length to width) of the thermal fields is about 1.2 in each case.

IV. THE STRUCTURE OF THE THERMAL AND VELOCITY FIELDS NEAR THE FREE SURFACE

In order to more clearly understand the processes involved in the transport of heat at the interface, a more detailed investigation of the relationship between the surface thermal field, and the subsurface velocity and vorticity was undertaken. In the case for which the free surface temperature is held constant, it is evident that the *flux* at the interface will vary spatially and temporally, its structure being determined by the subsurface hydrodynamics. On the other hand, for the constant flux case, the *surface temperature* field will fluctuate. Accordingly, a detailed visual and statistical analysis has been performed to determine the relationships between the thermal and hydrodynamic fields. It will be shown below that there are fundamental differences between the surface flux field in the constant temperature case and the surface temperature field in the constant flux case. In addition, a relatively simple physical model is offered which appears to explain these differences in a qualitative sense.

A. Visualizations of the near-surface structure

In Figs. 13(a)–13(d) several visualizations of the surface thermal and velocity fields at or near the free surface for the case in which the surface temperature field is fixed are shown. The fields are shown at the same instant in time so that relationships can be more easily determined. The mean flow is directed from left to right (positive x direction) in these visualizations. Each figure represents a fluctuating quantity in the sense that the instantaneous mean has been subtracted. In Fig. 13(a) the temperature field slightly below the interface is shown. It is evident that since the temperature field at the free surface is fixed ($\Theta^*=0$), these temperature fluctuations very near the surface are effectively proportional to the instantaneous surface flux. This is evident by noting the almost exact correspondence between the temperature fluctuations in Fig. 13(a) and the fluctuations in the flux at the interface shown in Fig. 13(d). The subsurface temperature field shows a strong positive skewness—in agreement with the statistical result (see Fig. 11)—exhibiting localized spots of high temperature. Although it may be difficult to discern from Fig. 13(a), the thermal structure has a some-

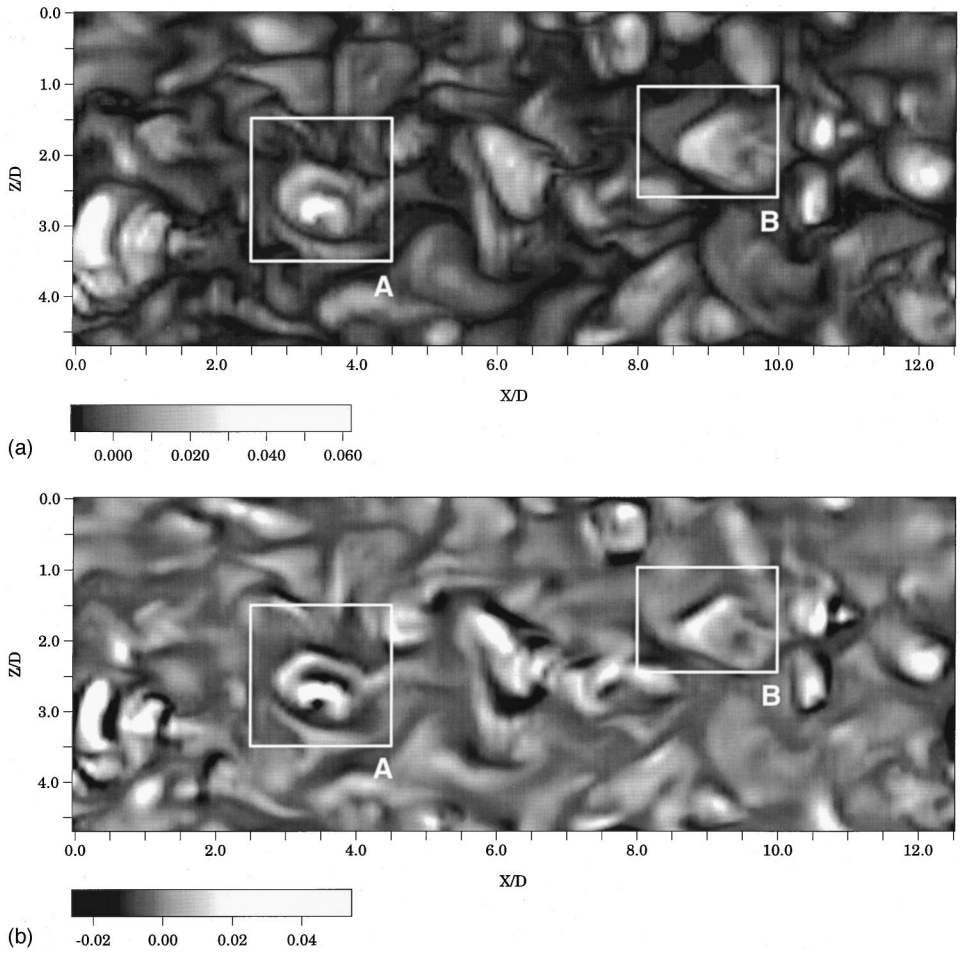

FIG. 13. Instantaneous visualizations of the thermal and velocity fields in the constant temperature case in the $x-z$ plane. (a) Temperature fluctuations, $(\Theta^*)'$, at $y^+=0.24$, where $\Theta^*=(\Theta-\Theta_T)/(|\Theta_B-\Theta_T|)$; (b) vertical velocity fluctuations, $(v^+)'$, at $y^+=0.24$; (c) streamwise velocity fluctuations, $(u^+)'$, at the free surface; and (d) flux fluctuations, $\partial(\Theta^*)'/\partial\overline{y}$, at the free surface.

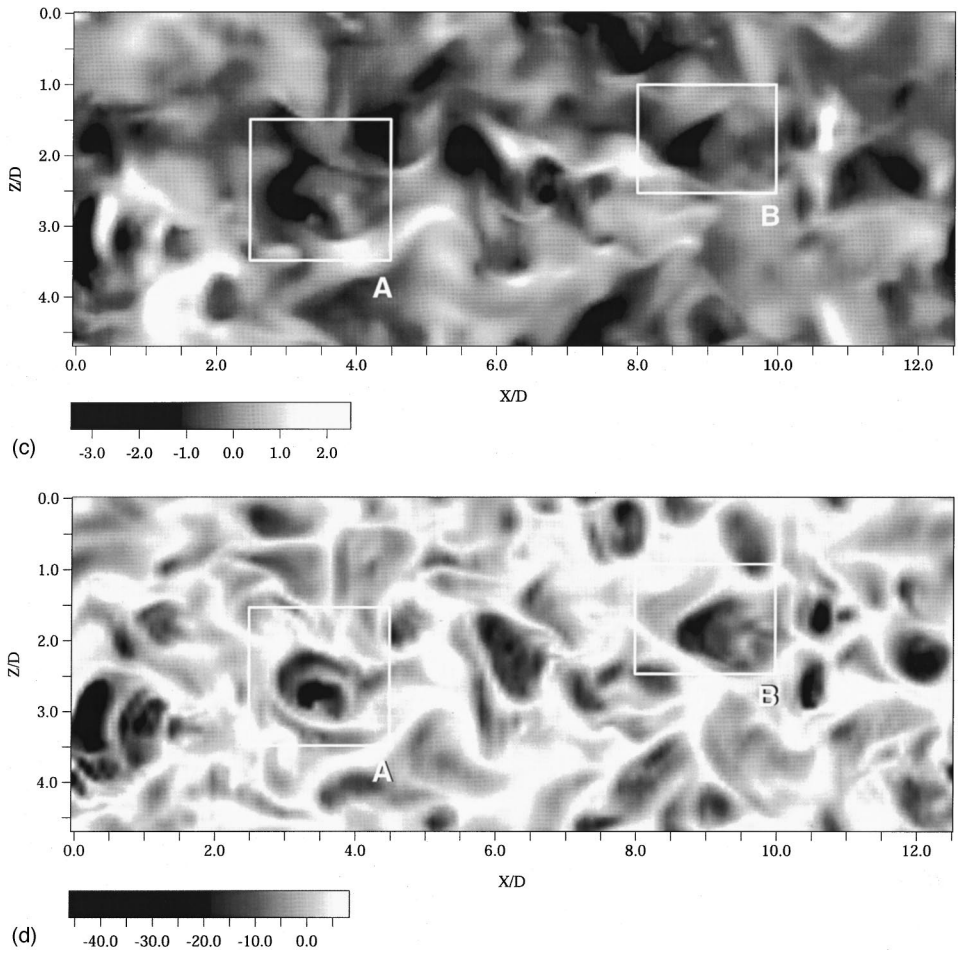

FIG. 13. (*Continued.*)

what larger streamwise length scale compared to its spanwise scale in accordance with the macroscale results mentioned previously.

In Figs. 13(b) and 13(c) the corresponding fluctuating vertical and streamwise velocity fields are shown. The vertical velocity field is taken very near the free surface, at the same depth as that of Fig. 13(a) for the temperature field. Regions A and B on each of these images have been highlighted. As indicated in Fig. 13(a), these are regions where the subsurface thermal temperature is strongly elevated and we term these regions *hot spots*. A close correspondence between these hot spots and large positive (upward) vertical velocity fluctuations is evident for these regions. The streamwise fluctuations shown in Fig. 13(c) show that *low speed* regions are also closely associated with the hot spots. It is also evident, upon close examination of many such visualizations, that the low speed regions appear generally slightly to the left, or *upstream* of these hot spots. The fluctuations in flux at the free surface shown in Fig. 13(d) show a strong negatively skewed and highly intermittent structure. Here, a negative value indicates heat transport out of the free surface. In fact, peak (outward oriented) fluxes are on the order of -40 compared to the mean flux of order -8.

The corresponding visualizations of the velocity and thermal fields for the case of constant surface heat flux is shown in Figs. 14(a)–14(d). The surface temperature in the constant flux case shown in Fig. 14(a) exhibits large *patches* of warm fluid which appear to be relatively uniform in temperature. The patches appear to be surrounded by regions of relatively intense cool bands, and, in fact, the overall skewness is slightly negative (see Fig. 11). The surface temperature field is strikingly different from the highly intermittent and positively skewed near-surface temperature field and surface flux shown in Figs. 13(a) and 13(d). In addition, the patches shown in Fig. 14(a) appear to show a definite *wake-like* structure, that is, a relatively large thermal *head* followed by a trailing *tail*. This is particularly apparent in the patches highlighted in region C. The corresponding vertical and streamwise velocity fields are shown in Figs. 14(b) and 14(c). As in the constant temperature case, there is an obvious correlation between the hot patches, large vertical velocities, and patches of low momentum fluid, as seen in region C. In addition, and in agreement with the constant temperature case, fluid with low streamwise momentum tends to appear somewhat upstream of the regions of high vertical velocity in areas where hot patches also appear on the surface.

The wake-like structure of the thermal fields in these two cases can be understood by considering the known surface flow kinematics. In accordance with the experimental observations described in the Introduction, and also in agreement with three-dimensional observations of the thermal and velocity fields obtained from these simulations (not shown), it

is known that eruptions of fluid from the wall region retain their coherence in the process of convecting toward the free surface. These upwellings eventually reach the surface as so-called splatting events. It seems reasonable to assume that these events are essentially composed of fluid carrying low streamwise momentum relative to the average velocity at the free surface since they have their origins in the buffer region of the mean velocity profile. In addition, in both the constant temperature and constant flux cases, heat is being transported from the solid wall toward the free surface, so that these fluid elements carry with them the higher temperatures associated with the subsurface flow, and must therefore be significantly warmer than the average surface temperature.

This transport of warm, low momentum fluid toward the free surface, as described above, explains the appearance of the thermal wakes; that is, in the same manner as a thermal wake is formed behind a warm solid object placed in a free stream, so too does a thermal wake form behind low momentum, warm fluid—*relative* to the average free surface streamwise velocity and temperature—as it impinges upon the free surface. This is certainly in agreement with the orientation of the thermal wakes noted above, in which the *head* is upstream and the *tail* downstream, with respect to the near-surface mean flow.

Recent experimental evidence[40–42] seems to confirm these observations. In the above cited experiments, a high-resolution infrared camera was used to obtain imagery of the temperature field of the free surface in a wind-wave tank under a variety of wind/current conditions. A strong constant heat flux at the free surface was obtained in these experiments primarily by wind-driven evaporative cooling. In this sense, the experiments were similar to the constant flux simulations. This induced the formation of a cool thermal boundary layer by generating rising warm plumes and sinking cool sheets. Thermal wake structures, referred to in the experiments as *fish scales*, readily formed as the ascending warm plumes encountered a wind-induced shear at the interface. These wake-like thermal patterns were more clearly evident in the experiments, compared to those in the present simulations, primarily because of the presence of surface shear which enhanced the formation of the thermal wakes and was also a source of significant turbulence production at the air–water interface. Nevertheless, the mechanism for the formation of a thermal wake structure at the interface is essentially identical in both cases. This has been further confirmed in recent simulations[43] in which surface shear has been applied to the interface. In these simulations, patterns almost identical to the cited experiments were formed.

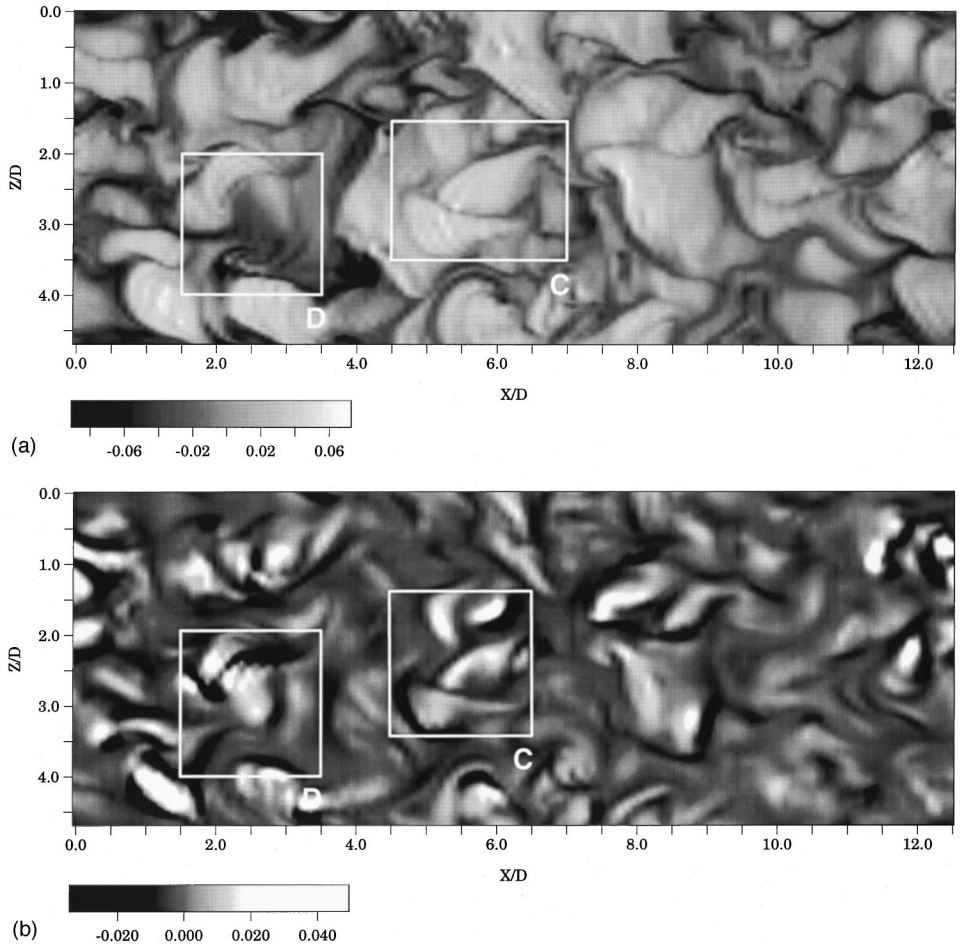

FIG. 14. Instantaneous visualizations of the thermal and velocity fields in the constant flux case in the $x-z$ plane. (a) Temperature fluctuations at the free surface, $(\Theta^*)'$, where $\Theta^*=[(\Theta-\Theta_B)k]/(q_0 D)$; (b) vertical velocity fluctuations, $(v^+)'$, at $y^+=0.24$; (c) streamwise velocity fluctuations, $(u^+)'$, at the free surface; and (d) flux fluctuations, $\partial(\Theta^*)'/\partial\overline{y}$, at $y^+=0.24$.

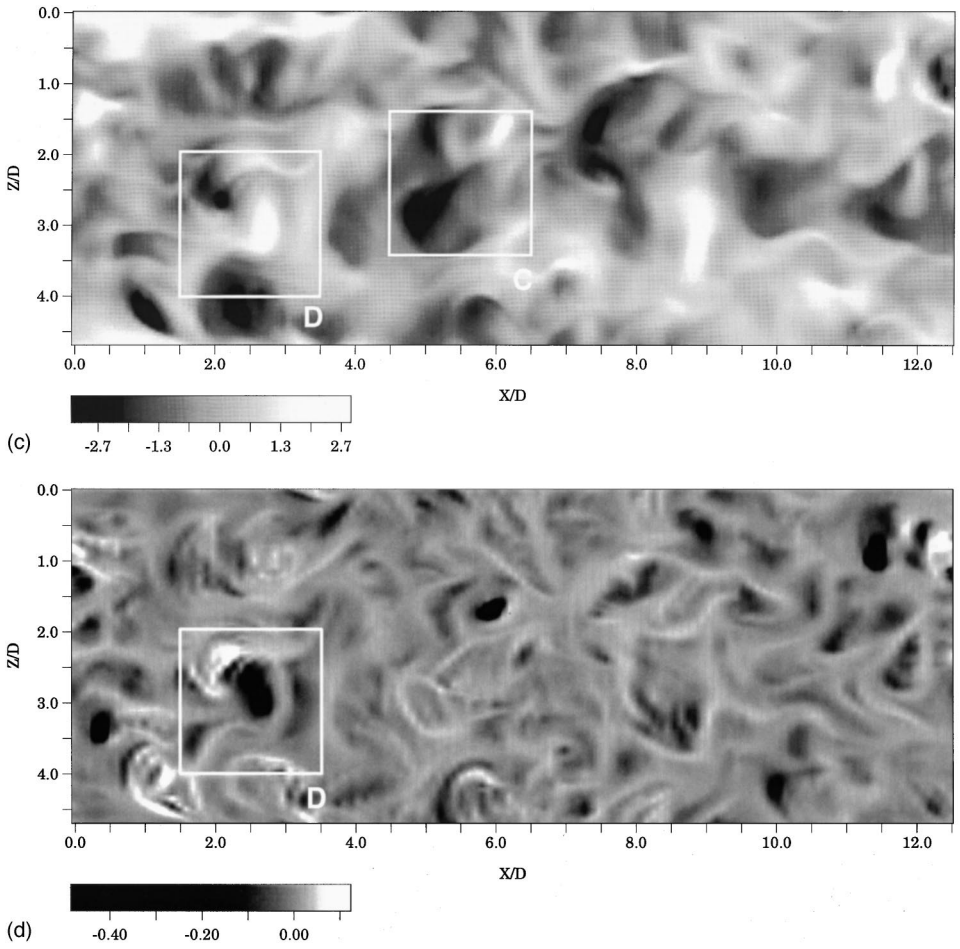

FIG. 14. (*Continued.*)

B. A two-time-scale model of surface renewal

The thermal structure revealed in Figs. 13 and 14 reveal significant differences between the surface flux field in the constant temperature case and the surface temperature field in the constant flux case in spite of the fact that the hydrodynamic fields are statistically identical. In particular, it was noted above that the surface flux field in the former was much more intermittent than the surface temperature field in the latter. Here a relatively simple model is proposed which appears to explain, in a heuristic manner, many of these differences. Certain simplifying assumptions are necessary in order to form a model which is more tractable than the full equations governing the system. Before proceeding, however, it is convenient to define a *thermal boundary layer* as the region near the free surface in which heat transport by molecular conduction dominates over turbulent transport. Referring to Fig. 8, the *average* thickness of this layer, δ_T/D, is on the order of 0.05 near the free surface.

To form such a model, the surface renewal process will be idealized by dividing it into a three step process: (1) the vertical velocity below the surface is initially small and the instantaneous thermal boundary layer is larger than δ_T; (2) the hydrodynamic straining field imposed by a surface renewal event compresses the thermal boundary layer to a thickness smaller than δ_T as v and the vertical strain rate, $\partial v/\partial y$, becomes large near the interface; and (3) the hydrodynamic field dissipates and the thermal boundary layer grows back to its original thickness by pure diffusion, completing the surface renewal process. The time period between steps (1) and (2) will be referred to as the compression or convective phase of the cycle, and has duration T_c. The third, diffusion-dominated phase has temporal duration T_d, and the sum of the time scales, $T_r = T_c + T_d$, is referred to as the surface renewal time.

The first assumption is that during the compression phase, diffusional effects are negligible. This can be seen by estimating the ratio of the dominant diffusion and convective terms in Eq. (2.7) for such a compression:

$$\frac{v\,\partial\Theta/\partial y}{\alpha\,\partial^2\Theta/\partial^2 y} \sim \frac{v\,\delta_T}{\alpha}. \tag{4.1}$$

In terms of the present simulations, a further estimate can be made:

$$\frac{v\,\delta_T}{\alpha} \sim \left.\frac{\partial v^+}{\partial \overline{y}}\right|_{\overline{y}=1} \left(\frac{\delta_T}{D}\right)^2 \left(\frac{u^* D}{\alpha}\right), \tag{4.2}$$

where $\partial v^+/\partial\overline{y}|_{\overline{y}=1}$ is the magnitude of the vertical derivative of the the free surface normal velocity at the interface which can reasonably be estimated from Fig. 3 as $\partial v_{\rm rms}/\partial\overline{y}|_{\overline{y}=1}$

~ 5. In addition, $u^*D/\alpha = R^*\mathrm{Pr} = 360$ so that $v\delta_T/\alpha \sim 5$, justifying, at least marginally, the assumption that diffusion can be neglected during the *initial* stages of boundary layer compression. It should be noted that if the compression phase has a long duration, that is, if $T_c \gg \delta_T/v$, the thermal boundary layer thickness will become small and then $v\delta_T/\alpha$ will no longer be large, so that at some point during the compression dissipative effects can no longer be neglected. However, if it is assumed that the compression phase lasts approximately one eddy turnover time near the interface, then $T_c \sim \lambda/v$, where λ is a typical velocity microscale near the interface. It follows that since $\lambda \sim \delta_T$ (obtained from calculations not shown), then $T_c \sim \delta_T/v$, and diffusion can reasonably be neglected throughout the entire compression of the thermal boundary layer. We note that even if this argument is not strictly valid, there will be some time period early in the compression phase for which diffusive effects will be entirely negligible.

It is useful to interpret this process as involving two time scales. These are referred to as the hydrodynamic straining scale, τ_h, associated with the compression of the thermal boundary layer due to a splatting event and a second scale, T_d, associated with the molecular diffusion of heat during recovery. These can be estimated as

$$\tau_h \sim \left(\left. \frac{\partial v}{\partial y} \right|_{fs} \right)^{-1} \tag{4.3}$$

and

$$T_d \sim \frac{(\delta_T)^2}{\alpha}. \tag{4.4}$$

Here, $\partial v/\partial y|_{fs}$ is the vertical strain rate at the free surface. It follows that

$$\frac{T_d}{\tau_h} \sim \frac{v\delta_T}{\alpha}, \tag{4.5}$$

in agreement with the estimate given above in (4.1). This indicates that the neglect of diffusion during compression can be interpreted as due to the existence of two disparate time scales. In effect, the time scale associated with the compression of the thermal boundary layer, τ_h, is significantly faster than the diffusional scale, T_d, associated with recovery. In addition, the thermal boundary layer thickness should decrease as the Prandtl number increases as $\delta_T \sim 1/\sqrt{\mathrm{Pr}}$ so that the time scale ratio given by (4.5) should *increase* as the square root of the Prandtl number. The scales for water ($\mathrm{Pr} \sim 7$), for example, will be significantly more disparate, and it is expected that in this case $T_d/\tau_h \sim 9$ at the Reynolds number of the current simulations.

To further simplify the model, it is assumed that during a typical splatting event, temperature gradients are negligible in the horizontal plane *near* the free surface; that is, the surface renewal events generates a wide, relative to its vertical extent, horizontally uniform patch of high temperature. In addition, all other variables are also assumed to depend only on y and t. Given these assumptions, the model equation for surface renewal becomes

$$\frac{\partial \Theta}{\partial t} + v\frac{\partial \Theta}{\partial y} = \alpha \frac{\partial^2 \Theta}{\partial^2 y}. \tag{4.6}$$

In the constant temperature case, the behavior of the flux at the interface may be determined by differentiating (4.6) with respect to y and evaluating this relation at the free surface. This results in

$$\frac{\partial Q_s}{\partial t} + \left. \frac{\partial v}{\partial y} \right|_{fs} Q_s = \alpha \left. \frac{\partial^2 Q}{\partial^2 y} \right|_{fs}, \tag{4.7}$$

where $Q_s(t)$ is the heat flux at the interface and $Q(y,t)$ is the heat flux. The term $v(\partial^2\Theta/\partial^2 y)$ drops out upon evaluation at the free surface due to the condition $v=0$ there.

Given the model described above, the structure of the thermal field near the free surface in the two cases under consideration can be readily determined. In the constant temperature case, since diffusion is negligible during the compression phase, and assuming the strain rate to be essentially constant in time, the right-hand side of (4.7) may be neglected and Q_s can be determined. This gives the simple result

$$Q_s(t) = Q_s(0)e^{(-\partial v/\partial y|_{fs} t)}. \tag{4.8}$$

Since the vertical strain rate at the free surface must be negative during such a splatting event, the surface flux must rise exponentially at a rate governed by the magnitude of the strain field. This can be interpreted as the process of generating a very thin interfacial thermal boundary layer as warmer fluid from below is driven upward. In the limit, as the layer becomes infinitely thin, the flux becomes unbounded. This is entirely consistent with classical surface renewal models[8,9] which start from the idealized initial condition of a discontinuous change in temperature at the interface which is intended to model bulk fluid coming into direct contact with a surface of fixed temperature or concentration. It is evident that (4.8) is consistent with the compression phase occurring on a fast time scale governed by the vertical strain rate, as described above. Another interpretation of this result is that in the absence of diffusion, fluid particles approaching the free surface from below must retain their initial temperature, so that the thermal boundary layer becomes thin and the flux rises on the time scale associated only with the kinematics of the flow. The splatting event then dissipates and the surface flux must decrease on a slow diffusional time scale as the thermal boundary layer thickens.

For the case in which the surface flux is held fixed, the scenario described above must be modified since the temporal behavior of the *surface temperature* is of concern. If diffusion is entirely neglected during the compression phase, then (4.6) evaluated at the free surface yields $\partial\Theta/\partial t|_{fs} \sim 0$. Naturally, there will be some temperature rise during this phase since diffusion is not entirely negligible, but within the approximation of the model, the rise should be small. During

compression, although the flux at the surface is fixed and the surface temperature rise is small, there must be an increase in *subsurface* flux as the thermal boundary layer is compressed. The subsurface heat flux rapidly becomes larger than the surface flux. Once the splatting event is dissipated, the surface temperature increases on a *slow* (diffusional) time scale due to this imbalance in interfacial flux. The surface temperature then decreases during the recovery period on the same slow time scale. It is clear that this is an idealization since the compression of the thermal boundary layer and heating of the surface go on simultaneously. Nevertheless, according to the model, the time required for the surface temperature to reach its maximum for the constant flux case should be considerably longer than the time needed for the flux to attain its maximum in the constant temperature case. In summary, the constant flux boundary conditions dictate that *diffusional* as well as convective effects must play important roles in surface heating, whereas for constant temperature conditions, diffusion is not necessary to produce large, very rapid increases in surface flux.

Evidence for this in given in Fig. 14(d) where the fluctuations in the instantaneous subsurface flux are shown for the constant flux case. It is evident that there are several regions in which the flux just below the interface is significantly larger (i.e., more negative) than the mean. One such region is indicated in region D which has been delineated also in Figs. 14(a)–14(c). It is evident from Fig. 14(a) that the region of high subsurface flux corresponds to an area in which the surface temperature *does not* significantly deviate from the mean. Figure 14(b) indicates that the high flux region also corresponds to a region of high subsurface vertical velocity directed toward the free surface. Close examination of Fig. 14(c) reveals that the region of high flux is located approximately midway between regions of large positive (downstream) and negative streamwise velocity fluctuations. These observations appear to be the same for the other regions in Fig. 14(d) in which there are large, outwardly directed, subsurface fluxes. The model described above suggests that during the compression stage, the surface temperature does not rise significantly. On the other hand, the subsurface straining sets up an interfacial flux imbalance which eventually leads to an increase in surface temperature on a diffusive time scale. This implies that, in regions where the subsurface flux is highly elevated, we are observing the *beginning* of a surface renewal event; that is, the initial stage of the compressive part of the process. The appearance of high and low streamwise momentum on either side of the high flux region is also expected as a *splat* tends to decelerate fluid upstream and accelerate it downstream.

In the constant temperature case, the model suggests that during the compressive phase of the process, the surface flux can rise rapidly to large magnitudes before diffusive effects have an appreciable effect. This seems to explain the significant intermittency in the flux field which is well reflected in the large skewness and flatness for v near the interface (see Figs. 6 and 7). On the other hand, the model also suggests that the intermittency in surface temperature should be weaker in the constant flux case since the temperature rise occurs on a much slower diffusive scale, and the horizontal $(x-z)$ spreading of the hot spot prevents the development of spatially localized regions of elevated temperature. This is also supported by the statistics (see Figs. 11 and 12). The model also predicts that the lifetime of a surface temperature hot spot in the constant flux case is likely to be longer than the lifetime of a high flux region in the constant temperature case. This can be explained, according to the model, by the fact that both the rise and decay of the surface temperature in the constant flux case occur on a slow diffusional time scale, whereas in the constant temperature case, only the decay of the surface flux occurs on the slow scale. This prediction is reasonably well supported by the significantly larger macroscale for the surface temperature in the flux case compared with the macroscale for the surface flux in the other case (see Sec. III B). In effect, since the surface temperature hot spots have a longer duration, they have more time to diffuse and the ambient surface turbulence acts longer to advect and mix the warmer fluid. This appears to be the origin of the so-called *fish scale* patches, alluded to above, that are observed in these simulations and in physical experiments.

C. Correlations between the surface thermal fields and the subsurface velocity and vorticity

The visualizations exhibited in Sec. IV A reveal a qualitative correlation between the surface thermal field and the subsurface velocity field in both the constant temperature and constant flux cases. To determine—in a more rigorous way—the nature and strength of these correlations, the two-point correlation function relating the thermal fields (flux or temperature) at the free surface to the *subsurface* velocity and vorticity field were computed. The appropriate correlation functions for the constant temperature case are defined by

$$C_x(x',y)=\frac{\langle q'(x-x',y_0,z)a'(x,y,z)\rangle}{q_{\mathrm{rms}}(y_0)a_{\mathrm{rms}}(y)} \tag{4.9}$$

and

$$C_z(z',y)=\frac{\langle q'(x,y_0,z-z')a'(x,y,z)\rangle}{q_{\mathrm{rms}}(y_0)a_{\mathrm{rms}}(y)}, \tag{4.10}$$

where $y_0=D$ is the vertical coordinate corresponding to the free surface, a' refers to a fluctuating component of velocity or vorticity, $q'=-k\partial\Theta'/\partial\overline{y}$ is the fluctuating part of the heat flux in the direction normal to the interface, and averaging is taken over the horizontal $(x-z)$ plane and over all realizations of the flow. Here C_x and C_z will be referred to as the the streamwise and spanwise correlations, respectively. With this definition of heat flux, a point on the free surface where $q'>0$ corresponds to a region where heat is leaving the free surface at a rate greater than the mean flux. In the constant flux case the correlations are defined exactly as above, except that q' is replaced by Θ' and q_{rms} by Θ_{rms}. It is important to note the consequences of the definitions of the correlation functions given above. As an example, we note that if a maximum in the correlation function appears at $x'>0$, this must be interpreted as meaning that the flux or temperature field must be shifted *upstream* with respect to the kinematic field to achieve this maximal correlation. In

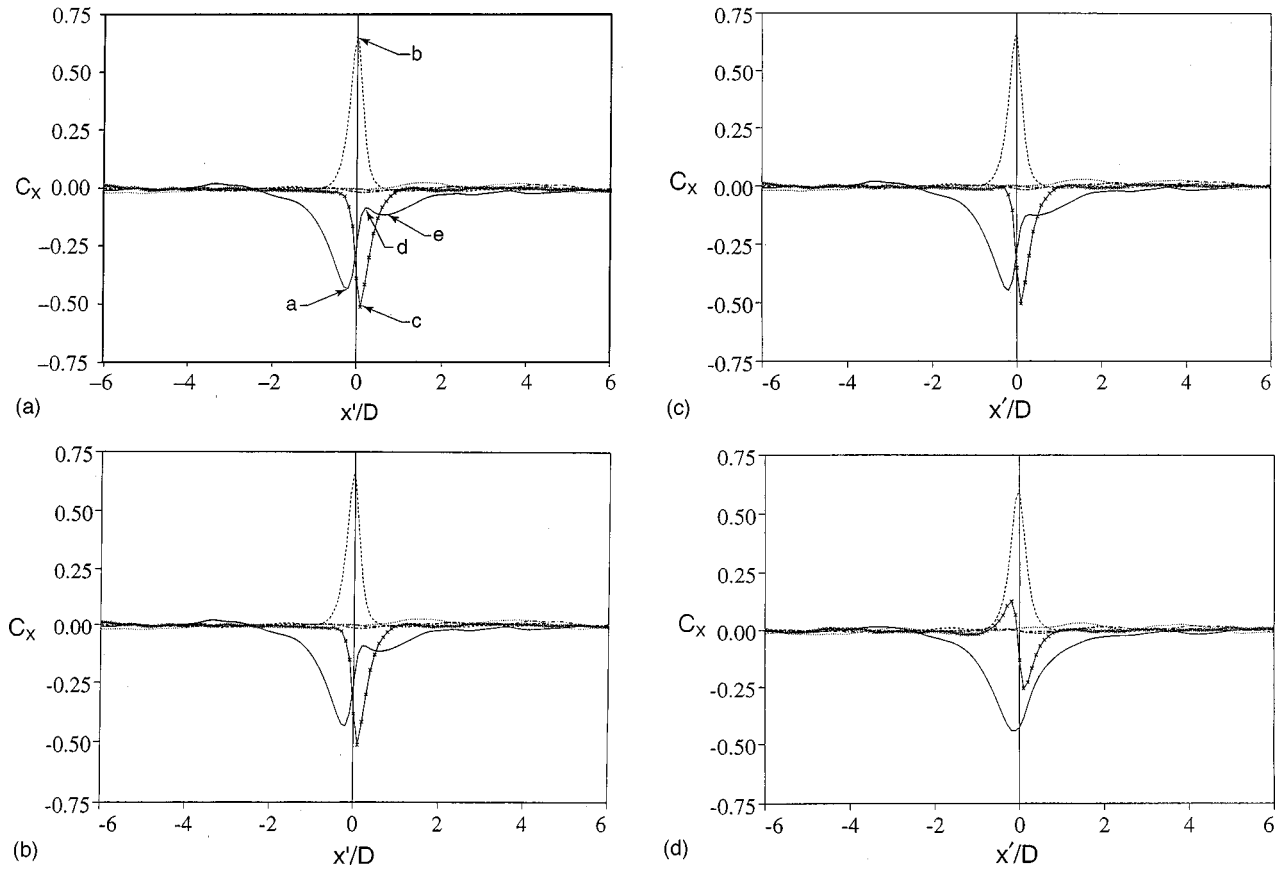

FIG. 15. Correlations of the heat flux at the free surface with the subsurface velocity and vorticity in the constant temperature case; (streamwise correlations). Correlations are defined in Eq. (4.9). Streamwise velocity, –; wall normal velocity, – – –; spanwise velocity,...; streamwise vorticity, -·-; wall normal vorticity, –·–; spanwise vorticity, ×. (a) $y^+=0.03$, (b) $y^+=2.2$, (c) $y^+=5.3$, and (d) $y^+=20.4$.

other words, the kinematic field can be thought of as *leading* the flux field in a spatial sense. We will therefore refer to $x'>0$ as upstream and $x'<0$ as downstream.

The streamwise correlation function for the constant temperature case is shown in Figs. 15(a)–15(d). Each figure is associated with a different y^+ location which refers to the distance below the surface where the velocity and vorticity fields are obtained to form the functions defined above. In Fig. 15(a), the result for the streamwise correlation is shown for the case in which the kinematic variables are very near the free surface ($y^+\sim 0.03$). Salient features of the correlations are indicated by the labels A–E. We note first that the surface flux is most strongly correlated with the vertical velocity and that the correlation is almost everywhere *positive* with a maximum value about 0.7 [see label B in Fig. 15(a)]. This maximum in the correlation occurs at or very near $x'=0$ and the correlation function also appears to be reasonably symmetric with respect its maximum. This appears to be more or less true independent of y^+ level as can be seen in Figs. 15(a)–15(d). In comparison, the correlation function for the streamwise velocity shows significantly different characteristics. As indicated by label A, the maximum value of this correlation is *negative* and occurs at $x'<0$, that is, *downstream* with respect to the flux. In addition, and somewhat unexpectedly, there is a local minimum and maximum indicated by labels D and E. The maximum correlation for the spanwise vorticity is strongly *negative* and occurs slightly *upstream* as indicated by referring to label C. It should be noted that this minimum in the spanwise vorticity correlation lies *upstream* of the maximum vertical velocity correlation (label B) and somewhat *downstream* of the local minimum for the streamwise velocity correlation (label D). The correlations for the spanwise velocity and the streamwise and vertical vorticity are near zero. This will be shown below to be consistent with the symmetries associated with a typical splatting event. At $y^+=5.3$ it is evident from Fig. 15(c) that the local minimum and maximum in the correlation for u have nearly vanished. At $y^+=20.4$, the correlation for u becomes more nearly symmetric about $x'=0$ and that for the spanwise vorticity tends towards antisymmetry. The spanwise correlations for the constant temperature case are shown in Figs. 16(a)–16(d). It is evident that, independent of depth, the spanwise correlations are either symmetric (u, v, and Ω_z) or antisymmetric (w,Ω_x,Ω_y) with respect to $z'=0$.

In Figs. 17(a)–17(d) the streamwise correlations for the constant flux case are shown. There are some differences worth noting between these results and those corresponding to the constant temperature case. In particular, the surface temperature field and the subsurface kinematic fields are substantially less correlated in this case compared to the much stronger correlation between the surface flux and the subsur-

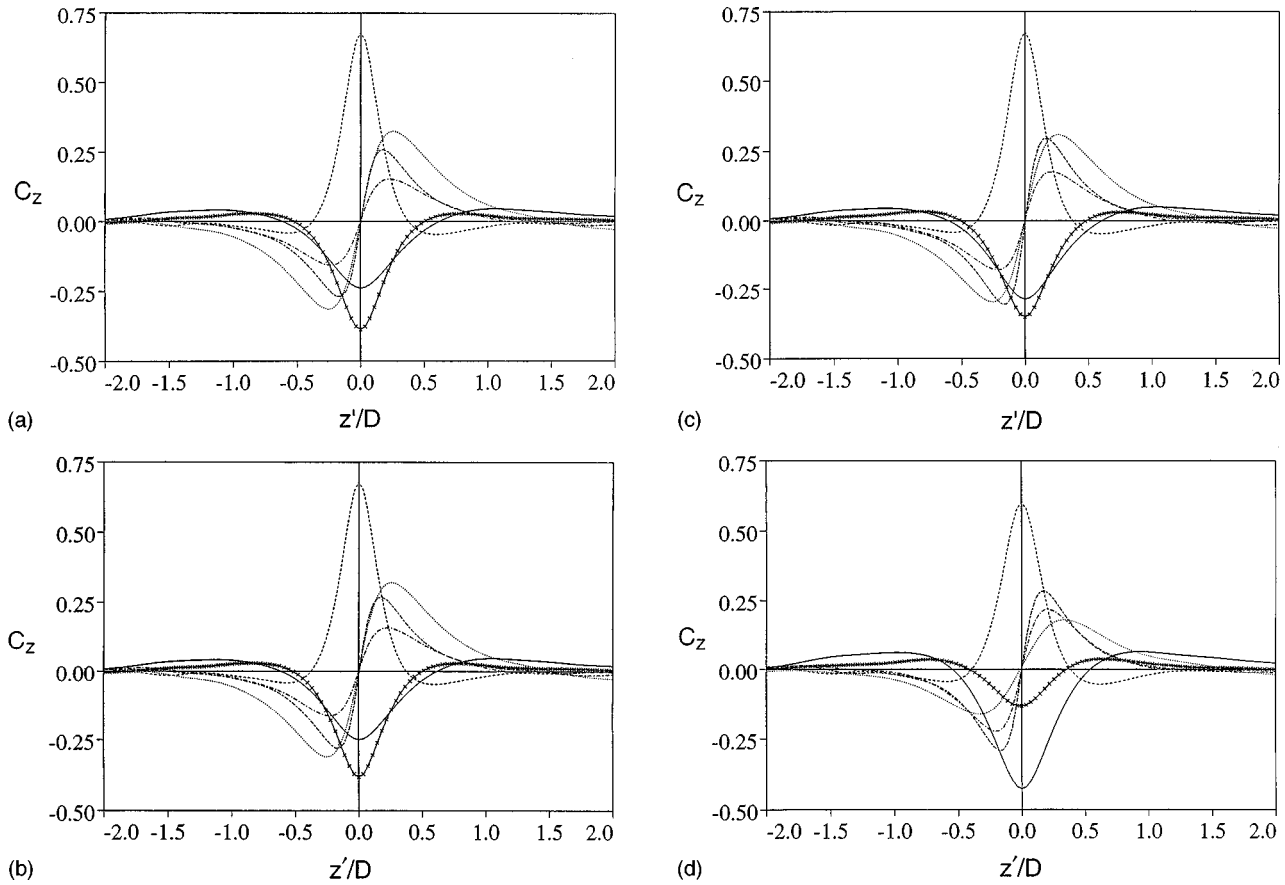

FIG. 16. Correlations of the heat flux at the free surface with the subsurface velocity and vorticity in the constant temperature case (spanwise correlations). Correlations are defined in Eq. (4.10). Streamwise velocity, –; wall normal velocity, ––; spanwise velocity, ⋯; streamwise vorticity, -·-; wall normal vorticity, –·–; spanwise vorticity, ×. (a) $y^+=0.03$, (b) $y^+=2.2$, (c) $y^+=5.3$, and (d) $y^+=20.4$.

face flow in the constant temperature case. For example, the maximum correlation coefficient for the vertical velocity from Fig. 17(a) is about 0.3 compared to 0.7 for the constant temperature case. In addition, the local minimum in the streamwise velocity correlation in Fig. 17(a) is not as clearly defined and has apparently shifted upstream in comparison to the local minimum labeled D in Fig. 15(a). The spanwise correlations for the constant flux case (not shown) are qualitatively the same as those for the constant temperature case and exhibit no new features.

D. Conceptual model for the typical surface renewal events

The visualizations and the correlations described above, along with the experimental observations that near surface splatting events arise from near-wall turbulent activity, point to the possibility that known coherent turbulent structures may be responsible for surface renewal. In particular, it is well known that *hairpin* eddies or parts of such eddies exist near the wall,[44–46] and that such eddies are dynamically capable of rising due to vortex self-induction. It is therefore reasonable to choose them as candidate structures. To determine whether such structures are consistent with the simulation results, a rough depiction of one and its associated velocity and thermal field is shown in Figs. 18 and 19. These depictions are intended to represent the flow only in the region very near the free surface. Both a side view (looking in the negative z direction) and a view looking in the direction of the flow are shown. In the side view the instantaneous velocity vectors expected for such an eddy in a reference frame translating with the mean velocity of the free surface is also indicated. Also included in Fig. 18 is a sketch of the surface flux (q') profile, appropriate for the constant temperature case, and the velocity (u',v') and spanwise vorticity (Ω_z') profiles that one would expect in a horizontal plane situated above the eddy. The profiles are taken along a cut corresponding to the plane of symmetry of the eddy; that is, along a line in the x direction formed by the intersection of the plane of symmetry with the horizontal plane (the $x-z$ plane indicated in the figures) above the eddy.

The depictions shown in Figs. 18 and 19 are naturally intended only to be suggestive of a typical hairpin eddy as it impinges onto the surface. The eddy is shown approaching the interface at some angle of attack, conforming to the expectation that the near-surface eddies should not differ significantly in their topology from the more well-characterized near-wall, tilted hairpin structures. From the numerical experiments cited above[45,46] it is well known that the near-wall eddies rarely appear with two *legs* of equally strong vorticity. In fact, they appear most often as single vortices. However, it is expected that since there is no preferred sense of

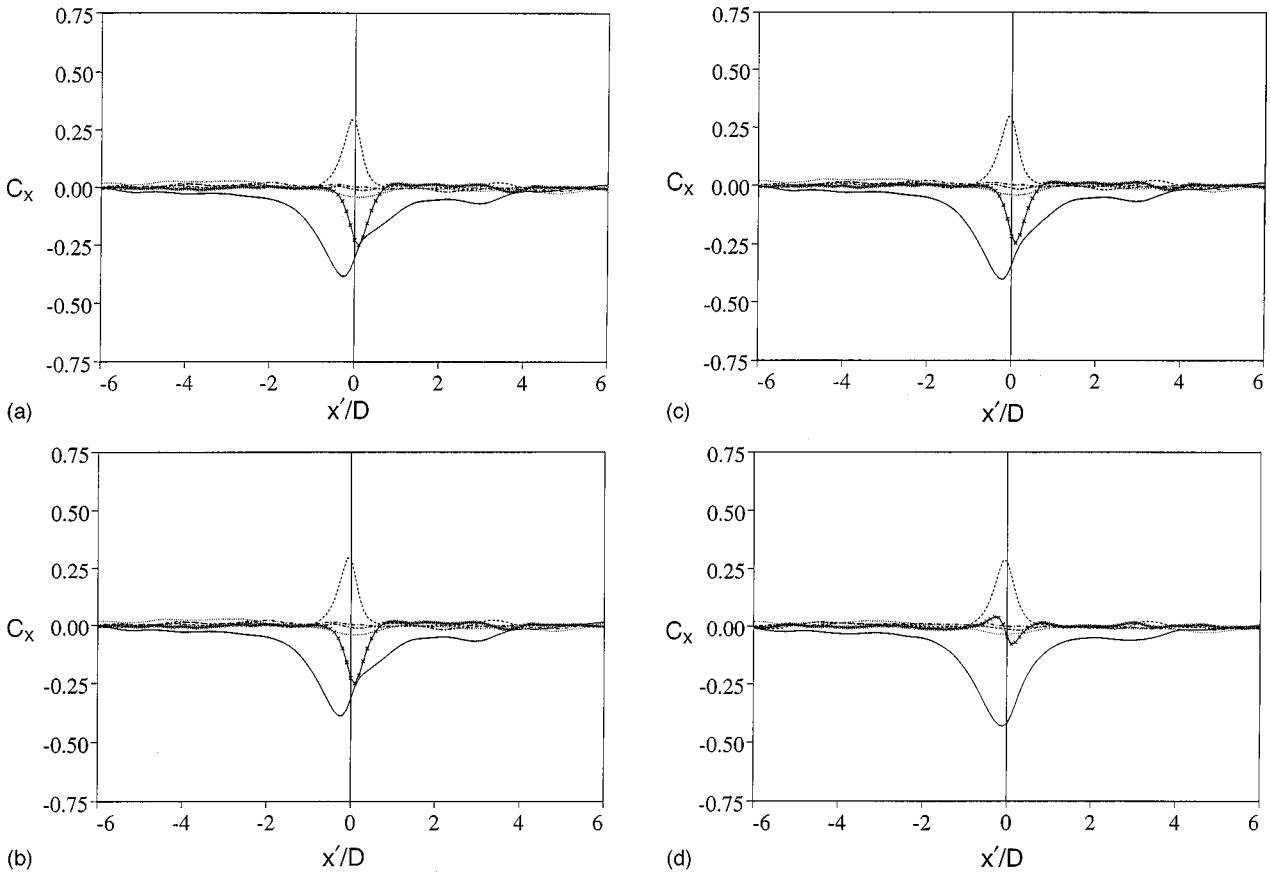

FIG. 17. Correlations of the temperature at the free surface with the subsurface velocity and vorticity in the constant flux case (streamwise correlations). Correlations are defined in Eq. (4.9). Streamwise velocity, –; wall normal velocity, – – –; spanwise velocity, ⋯; streamwise vorticity, -·-; wall normal vorticity, –·–; spanwise vorticity, ×. (a) $y^+=0.03$, (b) $y^+=2.2$, (c) $y^+=5.3$, and (d) $y^+=20.4$.

rotation associated with any given vortex, a statistical ensemble of such structures may appear as a two legged hairpin as depicted in the figure.

According to the discussion above, we should expect the maximum *positive* flux to be associated with the maximum *positive* vertical velocity since it is expected that here the thermal boundary should be thinnest after being compressed against the surface. This correspondence is indicated by label 2 in Fig. 18. Since the vortex is tilted in the manner shown, it is reasonable to expect that the maximum *negative* streamwise velocity should be located somewhat *downstream* of the maximum vertical velocity as indicated by label 1. At the *head* of the vortex, the spanwise vorticity is a maximum and must be negative there. This maximum should occur in the neighborhood of label 3 as indicated. It is clear that the other components of velocity and vorticity must be zero in this depiction because of the inherent spanwise symmetry of the flow field. Downstream of the head of the vortex the stream-

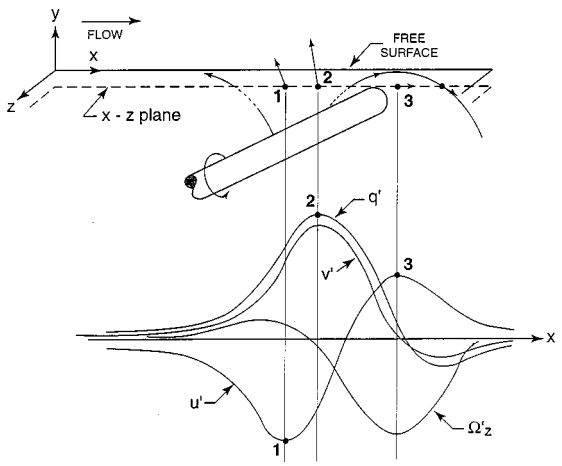

FIG. 18. Conceptual model of hairpin eddy impinging on the free surface. Side view ($x-y$ plane) showing velocity vectors as they would appear in a reference frame moving with the mean velocity of the free surface. Also shown are various field quantities in arbitrary units for the constant temperature case.

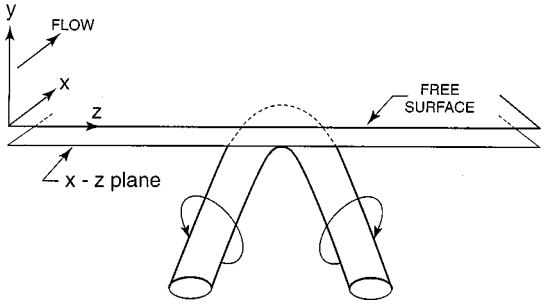

FIG. 19. Rear view ($z-y$ plane) of hairpin eddy impinging on the free surface.

wise velocity may be expected to be strongly positive, and the vertical velocity should be near zero, as indicated in Fig. 18 at label 3. Further downstream of this point, the flux should change sign since the thermal boundary layer should be larger than its mean thickness as it is pulled from the free surface toward the interior. This is typically referred to as an *antisplat* occurring *ahead* of the vortex tip.

Given these hypothetical hydrodynamic and flux fields, it is evident that the maximum correlation of the flux with the vertical velocity will be positive and should appear at $x' \sim 0$, in agreement with the computed correlations. The maximum correlation of the streamwise velocity should be negative appearing at $x' < 0$, and that for the spanwise vorticity should also be negative and should appear at $x' > 0$, also in agreement with the simulation results. The streamwise velocity and spanwise vorticity signatures are particularly important since they appear to be a characteristic of a *tilted* vortical structure. That is, the characteristics evident in the u and Ω_z correlations are not likely to manifest themselves as clearly in a splatting event generated by a vortical structure which approaches the surface at zero angle of attack. It is also important to note that this appears to explain the observations from the visualizations of the appearance of low streamwise velocity regions located somewhat downstream of regions of high vertical velocity. This proposed hydrodynamic field also hints at a possible explanation for the local minimum in the streamwise correlation function [see Fig. 15(a) and label D]. It is evident from Fig. 18 that if the flux profile is shifted upstream so that its maximum corresponds with the maximum in u' near label 3, then a cancellation effect should be expected and the appearance of a local minimum is possible. This suggests that the local minimum is a direct consequence of the close proximity of the vortex head to the free surface. In addition, the model appears to explain the observation noted in Sec. IV C that the maximum value for the spanwise vorticity correlation is in close proximity to this minimum [see Fig. 15(a)]. Farther from the surface [Fig. 15(d)] the correlations become more symmetric (or nearly antisymmetric in the case of the spanwise vorticity) with respect to $x' = 0$. This suggests that at about $y^+ \sim 20$, the detailed structure of the vortex head is not impressed upon the surface heat flux. Instead, the surface flux is correlated with an upwelling in a shear flow which is the prototypical splatting structure.

The model described above also applies well to the constant flux case. For example, the location of the maximum vertical velocity should correspond to the maximum positive surface temperature. Compared to the constant temperature case, however, the constant flux correlations are significantly lower compared to those in the constant temperature case, and, in addition, the local minimum in the u correlation is not as well defined. A definitive explanation for these differences is not immediately apparent. One possible explanation is that, according to the time scale model of surface renewal described above, the high-temperature surface patches should have a longer lifetime and should consequently be larger and more spatially diffuse compared to the surface flux in the constant temperature case. This allows the random surface turbulence to convect and, in a sense, *scramble* the surface temperature patches so as to decrease their coherence with the underlying, quasi-deterministic, splatting events. If the local minimum in the u correlation is closely associated with the vortex head, then this scrambling effect can be expected to decrease its impact on the surface temperature. In effect, the *details* of the subsurface velocity field are no longer well reflected in the surface thermal field.

It is evident from Fig. 19 that velocity and vorticity profiles taken in the spanwise direction above the hairpin will be either synmmetric (u', v', Ω_z') or antisymmetric $(w', \Omega_x', \Omega_y')$ with respect to $z' = 0$. Since the surface flux or surface temperature profiles will be symmetric, the correlations will have the same symmetry as the hydrodynamic field. It is clear that this in good agreement with the correlations shown in Figs. 16(a)–16(d).

V. CONCLUSIONS

Direct numerical simulations of scalar transport at a shear-free boundary have revealed that the thermal structure at the interface depends strongly on the nature of the boundary conditions imposed on the scalar field. In particular, it is found that the surface flux field is highly intermittent in the case for which the surface temperature is held fixed. On the other hand, when the surface flux is held fixed, the surface temperature field shows significantly less intermittency. The interfacial temperature field in this case appears in patches of relatively uniform temperature, forming wake-like, fish-scale patterns. These structures are highly reminiscent of those found in recent experiments where the air–water interfacial temperature was characterized using infrared imagery. It seems reasonable to assert, based on the present work, that these wake-like patterns are caused by the impacting of warm, low-speed fluid onto the free surface. The low-speed fluid then forms a thermal wake as it encounters higher-speed, cooler, free surface fluid.

These differences in intermittency and thermal structure are explained in terms of a two-time-scale model of surface renewal. In the model, the thermal boundary layer is viewed as being strained or compressed by the vertical velocity field on a fast hydrodynamic time scale and then reforms on a slow diffusional scale. According to the model, the surface flux in the constant temperature case rises rapidly on the fast scale, whereas the surface temperature rises principally on a diffusive scale when the surface flux is held fixed. The model also appears to explain the result that the macroscale associated with the surface temperature field is larger than that for the flux in the constant temperature case. In addition, it hints at an explanation for the result that surface temperature is significantly less correlated with the subsurface kinematics in the constant flux case, compared to the larger correlations found between the surface flux and the hydrodynamics in the constant temperature case.

The thermal structure of the interface was further explored by examining the correlations of the surface thermal fields with the subsurface velocity and vorticity. The straightforward method of correlation analysis has been particularly useful since the scalar field acts as a marker upon which the subsurface hydrodynamic fields are impressed.

The correlations reveal distinctive features which appear to be consistent with the presence of coherent hairpin eddies near the interface. This is not entirely unexpected since such structures are well known to dominate the physics in the near-wall region of the flow and are known to be advected toward the interface. On the other hand, the current work indicates that they seem also to be the dominant structures contributing to the transport of heat and mass in the open channel flow considered here. It is evident, however, that there may be other structures present at the interface which may play important roles in surface renewal. The role played by such structures can only be revealed by an investigation of the instantaneous, three-dimensional hydrodynamic and scalar fields, which is left for future work.

ACKNOWLEDGMENTS

This work was supported by the Office of Naval Research through the Naval Research Laboratory. We also acknowledge the generous support of the DOD High Performance Computing Program.

[1]M. Rashidi and S. Banerjee, ''The effect of boundary conditions and shear rate on streak formation and breakdown in turbulent channel flows,'' Phys. Fluids A **2**, 1827 (1990).
[2]K. Lam and S. Banerjee, ''On the condition of streak formation in a bounded turbulent flow,'' Phys. Fluids A **4**, 306 (1992).
[3]S. Komori, R. Nagaosa, and Y. Muramami, ''Turbulence structure and mass transfer across a sheared air-water interface in wind driven turbulence,'' J. Fluid Mech. **249**, 161 (1993).
[4]H. Nakagawa and I. Nezu, ''Structure of space-time correlations of bursting phenomena in open-channel flow,'' J. Fluid Mech. **104**, 1 (1981).
[5]S. Komori, H. Ueda, O. Fumimaru, and T. Mizushina, ''Turbulence structure and transport mechanism at a free surface in an open channel flow,'' Int. J. Heat Mass Transf. **25**, 513 (1982).
[6]S. Komori, Y. Murakami, and H. Ueda, ''The relationship between surface-renewal and bursting motions in an open-channel,'' J. Fluid Mech. **203**, 103 (1989).
[7]S. Komori, R. Nagaosa, and Y. Muramami, ''Mass transfer into a turbulent liquid across the zero-shear gas-liquid interface,'' AIChE. J. **36**, 957 (1990).
[8]R. Higbie, ''Rate of absorption of a pure gas into a still liquid during short periods of exposure,'' Trans. AIChE. **31**, 365 (1935).
[9]P. V. Danckwerts, ''Significance of liquid-film coefficients in gas absorption,'' Ind. Eng. Chem. **43**, 1460 (1951).
[10]G. E. Fortescue and J. R. A. Pearson, ''On gas absorption into a turbulent liquid,'' Chem. Eng. Sci. **22**, 1163 (1967).
[11]J. C. Lamont and D. S. Scott, ''An eddy cell model of mass transfer into the surface of a turbulent liquid,'' AIChE. J. **16**, 513 (1970).
[12]M. Rashidi and S. Banerjee, ''Turblence structure in free surface flows,'' Phys. Fluids **31**, 2491 (1988).
[13]M. Rashidi, G. Hetstroni, and S. Banerjee, ''Mechanisms of heat and mass transport at gas-liquid interfaces,'' Int. J. Heat Mass Transf. **34**, 1799 (1991).
[14]M. Rashidi, ''Burst-interface interactions in free surface turbulent flows,'' Phys. Fluids **9**, 3485 (1997).
[15]S. Komori, R. Nagaosa, Y. Murakami, S. Chiba, K. Ishii, and K. Kuwahara, ''Direct numerical simulation of three-dimensional open-channel flow with zero-shear gas-liquid interface,'' Phys. Fluids A **5**, 115 (1993).
[16]R. A. Handler, T. F. Swean, and R. I. Leighton, ''Length scales and the energy balance for turbulence near a free surface,'' AIAA J. **31**, 1998 (1993).
[17]Y. Pan and S. Banerjee, ''A numerical study of free surface turbulence in channel flow,'' Phys. Fluids **7**, 1649 (1995).
[18]R. Nagaosa and T. Saito, ''Turbulence structure and scalar transfer in stratified free-surface flows,'' AIChE. J. **43**, 2393 (1997).
[19]R. Nagaosa, ''The effect of the intermittent vortical structures on the scalar transfer at a free surface in open-channel flows,'' Proceedings of FEDSM'98, 1998 ASME Fluids Engineering Division (1998).
[20]R. J. Volino, G. B. Smith, R. I. Leighton, and W. Mckeown, ''Effect of a vortex pair on the temperature field at a free surface,'' Bull. Am. Phys. Soc. **41**, 1745 (1996).
[21]R. J. Volino and G. B. Smith, ''Use of simultaneous IR temperature measurements and DPIV to investigate thermal plumes in a thick layer colled from above,'' Exp. Fluids **27**, 70 (1999).
[22]T. D. Foster, ''Onset of convection in a layer of fluid cooled form above,'' Phys. Fluids **8**, 1770 (1965).
[23]L. N. Howard, ''Convection at high Raleigh number,'' in *Proceedings of the Eleventh Intl. Congress of Applied Mechanics, Munich, Germany*, edited by H. Gortler (Springer Verlag, Berlin, 1966), p. 1109.
[24]T. W. Liu and J. A. Businger, ''Temperature profile in the molecular sublayer near the interface of a fluid in turbulent motion,'' Geophys. Res. Lett. **2**, 403 (1975).
[25]K. B. Katsaros, W. T. Liu, J. A. Businger, and J. Tillman, ''Heat transport and thermal structure in the interfacial boundary layer measured in an open tank in turbulent free convection,'' J. Fluid Mech. **83**, 311 (1977).
[26]G. B. Smith, R. I. Leighton, and S. Tang, ''Infrared imaging of subsurface wake and thermal boundary layer interactions,'' Bull. Am. Phys. Soc. **42**, 2217 (1997).
[27]B. Jahne, K. O. Munnich, and U. Siegenthaler, ''Measurements of gas exchange and momentum transfer in a circular wind-water tunnel,'' Tellus **31**, 321 (1979).
[28]F. J. Ocampo-torres and M. A. Donelan, ''Laboratory measurements of mass transfer of carbon dioxide and water vapour for smooth and rough flow conditions,'' Tellus, Ser. B **46B**, 16 (1994).
[29]J. R. Saylor and R. A. Handler, ''Gas transport across an air-water interface populated with capillary waves,'' Phys. Fluids **9**, 2529 (1997).
[30]P. S. Liss, ''Processes of gas exchange across an air-water interface,'' Deep-Sea Res. Oceanogr. Abstr. **20**, 221 (1973).
[31]S. A. Orszag and A. T. Patera, ''Subcritical transition to turbulence in planar shear flows,'' in *Transition and Turbulence*, edited by R. E. Meyer (Academic, New York, 1981), p. 127.
[32]J. Kim, P. Moin, and R. Moser, ''Turbulence statistics in fully developed channel flow at low Reynolds number,'' J. Fluid Mech. **177**, 133 (1987).
[33]R. B. Dean, ''Reynolds number dependence of skin friction and other bulk flow variables in two-dimensional rectangular duct flow,'' J. Fluids Eng. **100**, 215 (1978).
[34]R. A. Handler, E. W. Hendricks, and R. I. Leighton, ''Low Reynolds number calculation of turbulent channel flow: a general discussion,'' Naval Res. Lab. Mem. Rep. 6410 (1989).
[35]B. Perot and P. Moin, ''Shear free turbulent boundary layers. Part1: physical insights into near-wall turbulence,'' J. Fluid Mech. **295**, 199 (1995).
[36]D. T. Walker, R. I. Leighton, and L. O. Garza-Rios, ''Shear-free turbulence near a flat free surface,'' J. Fluid Mech. **320**, 19 (1996).
[37]B. A. Kader, ''Temperature and concentration profiles in fully turbulent boundary layers,'' Int. J. Heat Mass Transf. **24**, 1541 (1981).
[38]J. Kim, ''Investigation of heat and momentum transport in turbulent flows via numerical simulations,'' in *Transport phenomena in turbulent flows: theory, experiment, and numerical simulation* edited by M. Hirata and N. Kasagi (Hemisphere, New York, 1988), p. 715.
[39]W. Tsai, ''Impact of a surfactant on a turbulent shear layer under the air-sea interface,'' J. Geophys. Res. **101**, 28557 (1996).
[40]G. B. Smith, R. I. Leighton, and S. Tang, ''Turbulent transition in the infrared,'' Phys. Fluids **10**, S9 (1998).
[41]G. B. Smith, R. I. Leighton, and S. Tang, ''An experimental and compuational investigation of the modulation of air-water interfacial temperature under varying conditions,'' Bull. Am. Phys. Soc., Div. of Fluid Dyn. **43**, 2017 (1998).
[42]R. I. Leighton, G. B. Smith, and S. Chen, ''Infrared imagery of wind waves,'' Bull. Am. Phys. Soc. **42**, 2217 (1997).
[43]R. A. Handler, R. I. Leighton, and G. B. Smith, ''Simulation of a sheared air-water interface with heat transfer,'' Bull. Am. Phys. Soc., Div. of Fluid Dyn. **43**, 2017 (1998).
[44]S. K. Robinson, ''Coherent motions in the turbulent boundary layer,'' Annu. Rev. Fluid Mech. **23**, 601 (1991).
[45]J. W. Brooke and T. J. Hanratty, ''Origin of turbulence-producing eddies in a channel flow,'' Phys. Fluids A **5**, 1011 (1993).
[46]P. S. Bernard, J. M. Thomas, and R. A. Handler, ''Vortex dynamics and the production of Reynolds stress,'' J. Fluid Mech. **253**, 385 (1993).